Journal of Applied Geophysics 251 (2026) 106325

Contents lists available at ScienceDirect

Journal of Applied Geophysics

journal homepage: www.elsevier.com/locate/jappgeo

Seismic characterization of water abundance in sandstone aquifers for mine water hazard prevention based on frequency-dependent response analysis

Hang Yu [a,b], Tongjun Chen [a,*], Luca de Siena [b], Heng Zhang [a], Haiyang Yin [a], Wan Li [a], Haicheng Xu [a]

[a] School of Resources and Geosciences, China University of Mining and Technology, Xuzhou 221116, Jiangsu, China
[b] Dipartimento di Fisica e Astronomia (DIFA), Alma Mater Studiorum-Università di Bologna, Bologna 40127, Italy

ARTICLE INFO

Keywords:
Seismic dispersion
Dispersion attribute
Roof sandstone aquifer
Water Hazard Prevention

ABSTRACT

Water in roof sandstone constitutes a significant concealed geological hazard, threatening the safe and efficient mining of coal resources. Geophysical prospecting is a key technical means for advanced detection of such hazards. Conventional electrical methods, while advantageous in detecting low-resistivity anomalies, are limited by their inability to identify complex structures, as well as by constrained investigation depth and spatial resolution. Meanwhile, traditional seismic approaches often overlook complex fluid-related dissipation mechanisms within strata. To address these limitations, this study proposes an integrated quantitative evaluation framework based on frequency-dependent rock physics modeling and seismic dispersion attribute inversion. First, a seismic rock physics model applicable to roof sandstone aquifers in Permian coal-bearing strata was established by integrating effective medium theory with Chapman's multiscale fracture model. Second, Sobol global sensitivity analysis was employed to quantify the contributions of key physical parameters to P-wave velocity (V_P) and inverse quality factor ($1/Q$). Subsequently, a forward model with four horizontal layers was constructed to comprehensively simulate reflection and interference effects in viscoelastic media, thereby establishing a theoretical relationship between water saturation (S_W) and the dispersion attribute (D_p). The forward modeling employed the propagator matrix method, using a 45 Hz Ricker wavelet as the source. In practical applications, high-resolution seismic spectra were obtained through the smoothed pseudo-Wigner-Ville distribution (SPWVD) combined with spectral balancing, and the dispersion attributes in the roof sandstone of the No. 4 coal seam were extracted using a frequency-scanning strategy. Sensitivity analysis indicates that, within the seismic frequency band, variations in V_P are primarily controlled by porosity, whereas $1/Q$ exhibits pronounced sensitivity to water saturation and fracture density. Seismic forward modeling further reveals a positive correlation between dispersion attributes and water saturation. Field results demonstrate that the spatial distribution of D_p attribute exhibits strong lateral heterogeneity, and D_p values show a significant positive correlation with hourly water yield measured at hydrogeological boreholes. These results confirm that the proposed approach enables the effective evaluation of sandstone aquifer water abundance using stacked seismic data, providing robust support for roof water hazard prevention. Moreover, for CO_2 geological storage (CCS) applications, the developed frequency-dependent rock-physics framework offers valuable constraints for reservoir characterization, site evaluation, and dynamic monitoring.

1. Introduction

As one of the primary geological disasters restricting the safe and efficient extraction of coal resources, mine water hazards have caused significant economic losses and social impacts, garnering intense attention from both the international academic community and industry (Dong et al., 2021; Wang et al., 2022). To address this challenge, electromagnetic exploration techniques, such as the transient electromagnetic method, high-density resistivity method, and controlled-source audio-frequency magnetotellurics, have been widely applied in mine hydrogeological investigations(Kouadio et al., 2022; Ritchie et al., 2024; Su et al., 2024; Ran et al., 2025). Although electromagnetic methods

* Corresponding author.
E-mail address: tjchen@cumt.edu.cn (T. Chen).

https://doi.org/10.1016/j.jappgeo.2026.106325
Received 23 January 2026; Received in revised form 10 May 2026; Accepted 12 May 2026
Available online 14 May 2026

possess unique advantages in identifying low-resistivity anomalous bodies, their inherent bottlenecks, including limited detection depth, insufficient coverage, and low spatial resolution in deep mining environments, have made the development of large-scale, quantitative, or semi-quantitative water hazard prediction techniques a critical scientific direction in current geophysical research(Strack, 2014; Xue et al., 2019; Metwally et al., 2022; El Hameedy et al., 2023; Hameedy et al., 2023; Allam et al., 2025).

Seismic exploration, owing to its high resolution and extensive coverage, has become the primary method for obtaining information on deep formations. Traditional fluid identification research primarily focuses on analyzing seismic attributes related to elastic characteristics. For instance, Fattahi and Karimpouli (2016) utilized artificial intelligence algorithms to optimize the prediction of water saturation in carbonate rocks using pre-stack seismic attributes; Fawad et al. (2020) compared multiple fluid identification schemes and quantitatively evaluated their sensitivities; Wang and Wang (2023) improved the prediction accuracy of gas hydrate reservoirs based on the Brekhovskikh equation; and Guo et al. (2022a) combined PP-wave azimuthal amplitude differences with hybrid optimization algorithms to achieve refined characterization of volcanic gas reservoirs. Furthermore; the new rock physics template proposed by Makarian et al. (2023); the novel fluid factor expression proposed by Farfour and Castagna (2024); and the classification scheme combining AVO with wave impedance attributes by Al-Ashqar et al. (2025) have achieved significant results in oil and gas field exploration. With the advent of 4D seismic technology; Huang et al. (2021) achieved the dynamic characterization of reservoir parameters by utilizing time-lapse pre-stack seismic attributes. With the rapid advancement of machine learning techniques; the integration of seismic attributes and well-logging data has further enabled robust and data-driven prediction of reservoir parameters; thereby expanding the methodological framework for quantitative reservoir characterization (Saleh et al., 2025a, 2025b, 2025c).

However, most of these methods are based on elastic media theory, making it difficult to accurately characterize complex fluid dissipation mechanisms within formations. When facing sandstone aquifers with strong heterogeneity and complex fluid occurrence conditions, identification methods that rely solely on elastic characteristics exhibit inherent limitations. Due to the mobility and viscosity of fluids, seismic waves exhibit significant frequency-dependent dispersion and attenuation characteristics when propagating through saturated sandstone, which establishes the rock-physics foundation for the quantitative evaluation of aquifers (Pang et al., 2019; Ba et al., 2023, 2025; Wei et al., 2024).

Models describing the dispersion and attenuation of porous media can be categorized into three major classes: macroscopic, mesoscopic, and microscopic. Macroscopic models, centered on Biot's theory(Biot, 1956); successfully simulate the wave characteristics of saturated rocks under high confining pressure; however; they suffer from significant prediction deviations at low effective pressure due to the neglect of microscopic pore structures. Microscopic models enhance applicability by introducing the squirt flow mechanism and combining rock anisotropy with viscoelastic features(Mavko and Nur, 1975; Yang and Zhang, 2002; Sun et al., 2020). Mesoscopic flow models provide a critical explanation for energy dissipation: when seismic waves excite pore pressure gradients at the mesoscopic scale, they induce the wave-induced fluid flow (WIFF) phenomenon(White, 1975; Ba et al., 2017; Yan et al., 2024). With advancing research, interlayer flow models, double-porosity models, and Chapman's multiscale fracture models have been proposed, broadening the application boundaries of the WIFF theory(Chapman et al., 2003; Chapman, 2003; Hu et al., 2022; Wei et al., 2023; Ba et al., 2025).

Regarding quantitative prediction, scholars worldwide have conducted extensive evaluations based on rock physics models and dispersion attribute inversion. Jin et al. (2018) utilized Bayesian inversion to obtain dispersion attributes and predict reservoir gas-bearing properties; whereas Ajaz (2021) inverted fracture-induced azimuthal anisotropic dispersion attributes through pre-stack data. Guo et al. (2022b) and Luo et al. (2023) significantly improved the identification accuracy of high gas-bearing zones by refining AVO inversion techniques and time-frequency analysis algorithms; respectively. Zhao et al. (2023) inverted interlayer dispersion attributes through frequency-dependent elastic impedance for precise fluid identification in tight sandstones. Guo et al. (2023) proposed a frequency-dependent seismic inversion method based on the effective fluid bulk modulus dispersion attribute; which leverages shale inelasticity to achieve the precise identification and characterization of hydrocarbon enrichment. Miao et al. (2025) proposed a dispersion-attribute estimation method that integrates pre-stack AVO inversion with a linear Bayesian framework; achieving accurate prediction of fluid distribution in thin sandstone reservoirs. Based on the characteristics of dispersive media; Zhu et al. (2025) constructed a fluid indicator derived from squirt-flow effects; enabling the discrimination of three oil-bearing reservoirs. Zhang et al. (2025) inverted azimuthal frequency-dependent dispersion attributes for vertical fracture characterization in orthorhombic shales via an amplitude-difference inversion scheme that incorporates fracture-induced anisotropy. In the field of hydrogeology; She et al. (2024) achieved high-precision prediction of the water-bearing properties of coal seam roof sandstone by considering temperature and pressure constraints.

Although extensive frequency-dependent rock physics research has been conducted worldwide, seismic rock physics has been only rarely been applied in China to predict sandstone water abundance, and the assessment of coal-seam sandstone water-bearing potential continues to face two major technical challenges: first, the transferability of existing petroleum reservoir models to the mine scale has not been fully verified; second, current frequency-dependent response analyses are mostly confined to single interfaces, ignoring the impact of water-bearing sandstone layer thickness and interlayer interference effects on the accuracy of synthetic records.

To address these issues, this study focuses on the roof sandstone aquifer of the No. 4 coal in the Hengyuan Coal Mine, constructs a Chapman multiscale rock physics model based on geological information, and quantitatively evaluates the contributions of key physical parameters to the P-wave velocity (V_p) and the inverse quality factor ($1/Q$) using Sobol global sensitivity analysis. To enhance the reliability of seismic response simulation, this study constructs a four-layer horizontal layered model and comprehensively characterizes reflection and interference effects in viscoelastic media using the propagator matrix method, thereby establishing a theoretical relationship between water saturation and the dispersion attribute. In the case study, the smoothed pseudo Wigner-Ville distribution (SPWVD) is employed to extract high-resolution seismic spectra, and spectral balancing is utilized to eliminate wavelet interference, followed by the extraction of the dispersion attribute of the roof sandstone aquifer using the frequency scanning method. Validation data from logging and hydrogeological boreholes demonstrated a robust positive correlation between dispersion attributes and sandstone water abundance, thus verifying the accuracy and practical feasibility of the proposed methodology. This study proposes a novel quantitative evaluation framework for detecting water hazard sources in roof sandstone prior to coal mining, thereby supporting safe and efficient mine production.

2. Geological settings

The study area is located in the Hengyuan Coal Mine of the central Huaibei Coalfield, which exhibits geological characteristics typical of the North China Coal-accumulating area (Fig. 1a). The region is characterized by a flat topography, with surface elevations ranging from +28.98 to +36.45 m. Structurally, the area is characterized by a monoclinal fold structure trending NNW direction and dipping NNE direction. Faults are predominantly developed in the NE, NNE, and NEE directions, and the formation dip angles generally range from 8° to 12°.

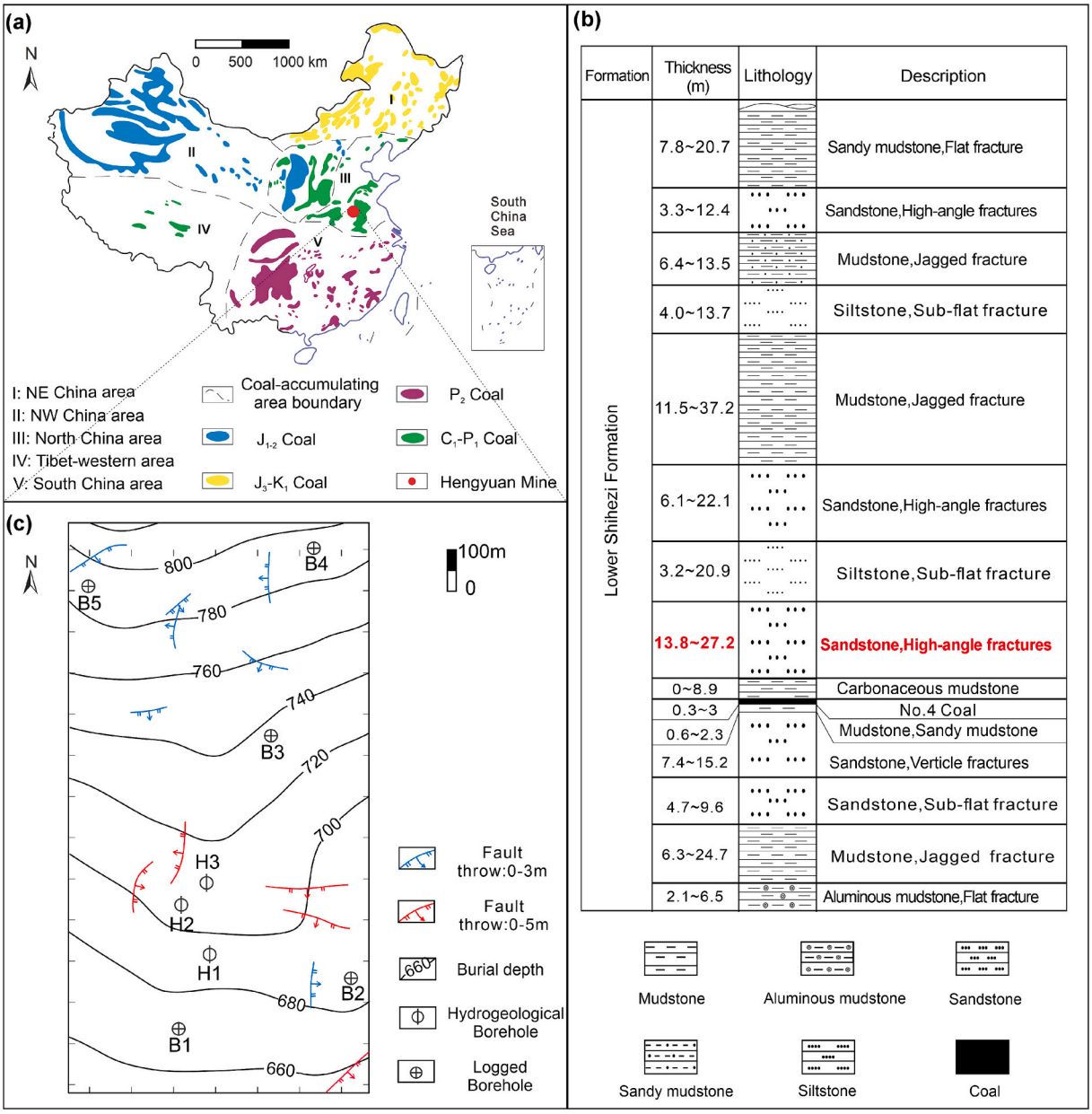

Fig. 1. (a)Location and geological structures of the study area, (b)Stratigraphic column of the coal-bearing strata, (c)Contour map of the floor of the No. 4 coal seam roof sandstone.

The stratigraphic succession in the study area, in ascending chronological order, comprises the Ordovician, Carboniferous, Permian, Neogene, and Quaternary systems. The primary coal-bearing strata reside within the Lower Shihezi Formation. This formation is lithologically dominated by mudstone and siltstone, featuring intercalations of medium to fine-grained sandstone. It contains 1 to 3 coal seams in total, with the No. 4 seam being the primary recoverable target. The stratigraphic column detailing the coal-bearing strata is presented in Fig. 1b. (See Fig. 2.)

The complex hydrogeological environment represents one of the core challenges confronting the safe extraction of the No. 4 coal seam in the Hengyuan Coal Mine. The No. 4 coal seam is buried at a relatively great depth, ranging from 662.6 to 842.7 m. Comprehensive hydrogeological investigations, including transient electromagnetic surveys and hydrogeological boreholes, have been conducted. The results indicate that fracture water within the No. 4 coal roof sandstone, located approximately 10 m above the seam, is relatively abundant and constitutes a potential direct source of water inrush. While the structural framework of the No. 4 coal roof in the study area is relatively simple and primarily characterized by small-scale secondary faults with throws of less than 5 m (Fig. 1c), core identification results reveal the extensive development of numerous high-angle to vertical tectonic fractures within the sandstone layers. Under the intense perturbation of deep-seated high in-situ and mining-induced stresses, these fracture systems are highly susceptible to forming interconnected water-conducting conduits, which subsequently evolve into roof dripping or catastrophic water inrush disasters.

3. Methods and workflow

3.1. Research concept and workflow

The roof sandstone of the No. 4 coal seam in the Hengyuan Coal Mine is characterized by deep burial and the prevalence of high-angle fractures. The abundance of fracture water and its tendency to form

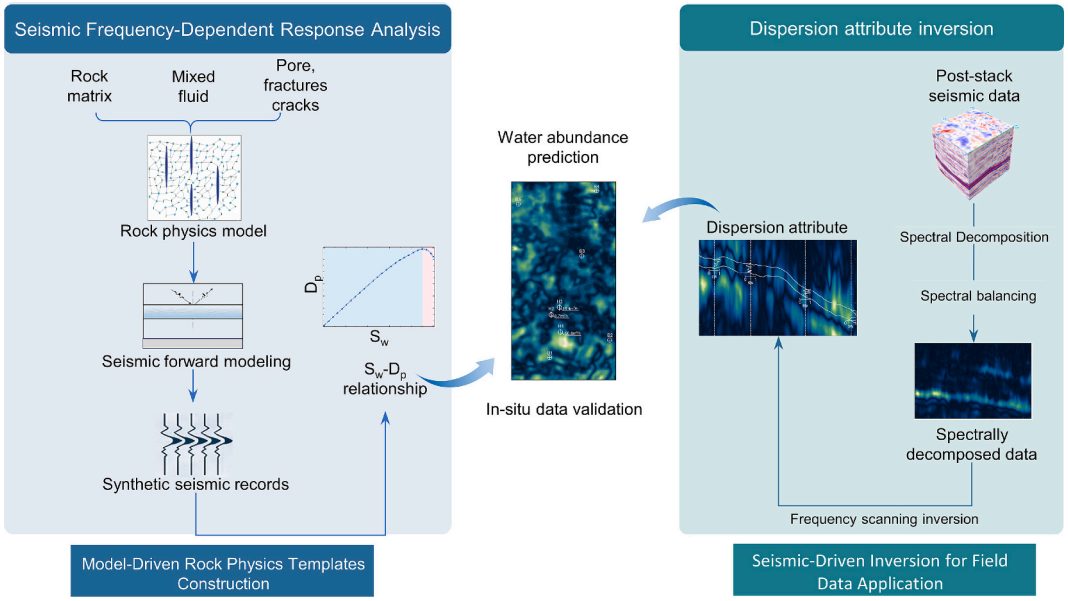

Fig. 2. Integrated workflow for water abundance prediction in sandstone aquifers based on seismic frequency-dependent response analysis.

interconnected flow conduits increases the risk of water inrush. Under such complex hydrogeological conditions, conventional seismic data (narrow azimuthal distribution) and its interpretation methods struggle to quantitatively evaluate aquifer water abundance, particularly because frequency-dependent seismic responses associated with fracture–fluid interactions are not fully utilized. Accordingly, a comprehensive workflow integrating rock physics modeling, seismic forward simulation, time–frequency analysis, and dispersion attribute inversion is developed. A broadband rock physics model capable of representing complex reservoir features is first constructed by considering the rock matrix, fluid mixtures, and the development of pores, fractures, and microcracks. Subsequently, seismic forward modeling is performed for sandstone formations under varying water saturation conditions using the propagator matrix method, and dispersion attributes are then inverted from the synthetic records to establish a theoretical relationship between water saturation and dispersion attributes. In the case study, the SPWVD time-frequency analysis method was introduced to obtain high-resolution seismic spectra while utilizing spectral balancing techniques to eliminate the adverse effects of wavelet overprinting. Ultimately, the model-driven theoretical relationships between water saturation and seismic dispersion attributes were integrated with the seismic data-driven dispersion attributes to predict the water abundance of the roof sandstone and validated against in-situ hydrogeological data from boreholes. This integration achieved a precise prediction of water abundance in the roof sandstone of the No. 4 coal seam.

3.2. Rock physics modeling for sandstone aquifer

Broadband rock physics modeling serves as a critical bridge linking intrinsic rock physical properties with seismic frequency-dependent response characteristics, representing the principal methodology for analyzing seismic rock physics signatures. The Chapman model comprehensively incorporates microscopic pores, microcracks, and mesoscopic fractures to characterize the fluid-induced dispersion and attenuation mechanisms within multiscale fracture systems, and has thus been widely adopted for the rock physics modeling of fractured, fluid-saturated rocks(Chapman et al., 2003). According to the Chapman model, the stiffness matrix of a sandstone aquifer can be calculated using the following equation:

$$C_{ij}(\omega) = C_{ij}^{(\mathrm{iso})} - \varepsilon_c C_{ij}^{(1)}(\omega) - \phi_{\mathrm{p}} C_{ij}^{(2)}(\omega) - \varepsilon_f C_{ij}^{(3)}(\omega) \tag{1}$$

where $C_{ij}^{(\mathrm{iso})}$ denotes the elastic stiffness matrix of the rock matrix; $C_{ij}^{(1)}$ denotes the elastic correction term induced by microcracks; $C_{ij}^{(2)}$ is the elastic correction term attributed to pores; $C_{ij}^{(3)}$ is the elastic correction term resulting from mesoscopic fractures; ε_c is the microcrack density; ϕ_{p} is the porosity; ε_f is the fracture density; and ω is the angular frequency. The formulas for calculating the stiffness constants are given in Appendix A.

Given that the Chapman model assumes a vertical transverse isotropy (VTI) medium, whereas the sandstone aquifer investigated in this study features high-angle to vertical fractures and microcracks, the formation conforms to the horizontal transverse isotropy (HTI) symmetry. Consequently, a Bond transformation must be applied to the elastic stiffness matrix to account for this change in symmetry(Yu and Chen, 2025).

Finally, the frequency-dependent P-wave velocity $V_p(\omega)$, S-wave velocity $V_s(\omega)$, and quality factor $Q(\omega)$ are determined according to the following expressions:

$$V_p(\omega) = \sqrt{\frac{C_{33}(\omega)}{\rho_s}}, V_s(\omega) = \sqrt{\frac{C_{44}(\omega)}{\rho_s}} \tag{2}$$

$$Q_p(\omega) = \frac{\mathrm{Re}(C_{33}(\omega))}{\mathrm{Im}(C_{33}(\omega))} \tag{3}$$

$$\rho_s = (1-\phi_{\mathrm{p}})\rho_m + \phi_{\mathrm{p}}(1-s_w)\rho_g + \phi_{\mathrm{p}} s_w \rho_w \tag{4}$$

where V is the complex velocity; $C_{33}(\omega)$ denotes the frequency-dependent stiffness coefficients; the imaginary and real parts of the complex modulus are denoted by Im and Re, respectively. ρ_m is the density of the rock matrix; ρ_g is the density of air; ρ_w is the density of pore water; s_w is the water saturation.

3.3. Seismic forward modeling

Conventional methods for calculating seismic reflection responses typically rely on the Zoeppritz equations to determine reflection coefficients at a single interface; however, by neglecting reservoir thickness, viscoelastic properties, and multi-layer wavefield interference, these approaches fail to meet the requirements for high-fidelity forward

modeling in dispersive media. The seismic forward modeling approach proposed by Carcione(Carcione, 1997, 2001, 2022); based on the propagator matrix method; ensures numerical stability while accurately characterizing P- and S-wave reflection and transmission; inter-layer interference; and thin-bed tuning effects within multi-layered anisotropic viscoelastic media; making it a widely adopted tool for simulating seismic responses in viscoelastic layers(Guo et al., 2022c; Miao et al., 2025).

Based on the seismic modeling method proposed by Carcione, the reflection and transmission coefficient matrix **r** for incident P-waves is calculated using the propagator matrix method, as follows:

$$r = -[A_1 - BA_2]^{-1} i_P \tag{5}$$

where $r = \left[R_{pp}, R_{ps}, T_{pp}, T_{ps}\right]^{\mathrm{T}}$, whose first element $R_{pp}(f)$ denotes the P-wave reflectivity coefficient. $\mathbf{A_1}$, $\mathbf{A_2}$, and **B** represent the propagator matrices of the upper, lower, and intermediate media, respectively. i_P is the incident P-wave vector. Detailed calculation procedures for these propagator matrices are provided in Appendix B.

For a given incidence wavelet, its frequency spectrum *W(f)* is computed via the Fourier transform; the governing equation is as follows:

$$W(f) = \int_{-\infty}^{\infty} \omega(t) e^{-i2\pi ft} dt \tag{6}$$

where $\omega(t)$ is the incident wavelet in the time domain, i denotes the imaginary unit, and f is the frequency.

The frequency-domain reflection amplitude spectrum $U(f)$ is determined by calculating the product of the frequency-dependent reflection coefficient and the incident wavelet spectrum:

$$U(f) = W(f) \times R_{pp}(f) \tag{7}$$

The inverse Fourier transform is applied to the reflection amplitude spectrum to reconstruct the seismic reflection record *u(t)*:

$$u(t) = \int_{-\infty}^{\infty} U(f) e^{i2\pi ft} df \tag{8}$$

3.4. Frequency-dependent amplitude versus frequency inversion

For near-normal incidence of seismic waves, the approximate expression for the frequency-dependent reflection coefficient is given by:

$$R_{PP}(\theta, f) \approx \frac{1}{2}\left(\frac{\Delta v_p(f)}{\overline{v_p(f)}} + \frac{\Delta \rho}{\overline{\rho}}\right) + \left(\frac{1}{2}\frac{\Delta v_p(f)}{\overline{v_p(f)}} - \frac{\Delta v_S(f)}{\overline{v_s(f)}} - \frac{1}{2}\frac{\Delta \rho}{\overline{\rho}}\right)\sin^2\theta \tag{9}$$

where $R_{PP}(\theta)$ denotes the reflection coefficient at an incidence angle θ; $\overline{v_p}$ represents the average P-wave velocity in the vertical direction across the interface; $\overline{v_s}$ signifies the average S-wave velocity in the vertical direction; $\overline{\rho}$ is the average density of the media on both sides of the interface; Δ represents the difference in physical parameters across the interface.

Given that post-stack data primarily characterizes the reflection response at near-normal incidence, where the incidence angle remains minimal, the aforementioned equation can be further reduced to:

$$R_{PP}(f) \approx \frac{1}{2}\left(\frac{\Delta v_p(f)}{v_p(f)} + \frac{\Delta \rho}{\rho}\right) \tag{10}$$

By designating the dominant seismic frequency as the reference frequency f_{ref}, a first-order Taylor series expansion of the aforementioned expression about f_{ref} yields:

$$R_{PP}(f) \approx \frac{\Delta v_p}{2v_p}\left(f_{ref}\right) + \left(f - f_{ref}\right)\frac{d}{df}\left(\frac{\Delta v_p}{2v_p}\right) + \frac{\Delta \rho}{2\rho} \tag{11}$$

Subtracting the expression for the frequency-dependent reflection coefficient at the reference frequency f_{ref} from the corresponding expression at frequency f yields:

$$\frac{R_{PP}(f) - R_{PP}\left(f_{ref}\right)}{f - f_{ref}} \approx \frac{d}{df}\left(\frac{\Delta v_p}{2v_p}\right) \tag{12}$$

The dispersion attribute, D_p, is defined as $D_p = \frac{d}{df}\left(\frac{\Delta v_p}{v_p}\right)$. Subsequently, Eq. (14) can be recast into the following matrix representation:

$$\begin{bmatrix} R_{PP}(t,f_1) - R_{PP}(t,f_0) \\ R_{PP}(t,f_2) - R_{PP}(t,f_0) \\ \vdots \\ R_{PP}(t,f_m) - R_{PP}(t,f_0) \end{bmatrix} = \frac{1}{2}\begin{bmatrix} f_1 - f_0 \\ f_2 - f_0 \\ \vdots \\ f_m - f_0 \end{bmatrix} D_{\mathrm{p}} \tag{13}$$

By employing the ridge regression algorithm(Hoerl and Kennard, 1970) to solve the linear system in Eq. (15), the dispersion attribute is effectively estimated as follows:

$$D_p = 2\left(G^T G + \lambda I\right)^{-1} G^T d \tag{14}$$

where $\boldsymbol{G}$ is defined as $\begin{bmatrix} R_{PP}(t,f_1) - R_{PP}(t,f_0) \\ R_{PP}(t,f_2) - R_{PP}(t,f_0) \\ \vdots \\ R_{PP}(t,f_m) - R_{PP}(t,f_0) \end{bmatrix}$, $\boldsymbol{G}^T$ denotes the transpose of matrix $\boldsymbol{G}$, λ represents the damping parameter, $\boldsymbol{d}$ is the observation vector, formulated as $\begin{bmatrix} (f_1 - f_0) \\ (f_2 - f_0) \\ \vdots \\ (f_m - f_0) \end{bmatrix}$, and f_m signifies the m-th target frequency.

As field seismic exploration yields non-stationary time-domain records, high-precision spectral decomposition is essential for resolving the frequency-dependent characteristics of reflection coefficients. In this study, the Smoothed Pseudo Wigner-Ville Distribution (SPWVD) was adopted due to its ability to provide superior joint time-frequency resolution while effectively mitigating the cross-term interference inherent in the standard Wigner-Ville Distribution. This high resolution is particularly critical for accurately extracting the dispersion attribute, as the inversion process relies on the subtle energy gradients across different frequency components. Compared with traditional methods such as the Short-Time Fourier Transform (STFT), which is limited by a fixed window length, SPWVD more precisely represents instantaneous frequency variations without the smearing effect. Methods with lower resolution, like STFT, tend to smooth out key frequency features, which can lead to reduced accuracy in the D_p inversion results. While Wavelet Transforms are effective for multi-scale analysis, they often lack the instantaneous frequency precision required for high-fidelity D_p estimation(Chakraborty and Okaya, 1995; Wu and Liu, 2009; Ajaz, 2021; Guo et al., 2022c). Therefore, SPWVD offers a balanced and robust approach for characterizing fluid-induced frequency-dependent seismic responses. The formulation of SPWVD is given by:

$$S(t,f) = \int_{-\infty}^{+\infty}\int_{-\infty}^{+\infty} g(u)h(\tau)x\left(t + \frac{\tau}{2} - u\right)x^*\left(t - \frac{\tau}{2} - u\right)e^{-j2\pi f\tau} du d\tau \tag{15}$$

where $g(u)$ denotes the smoothing window function in the time direction; $h(\tau)$ signifies the smoothing window function in the lag direction; $x(t)$ represents the seismic record to be analyzed; and $x^*(t)$ corresponds to the complex conjugate of the seismic record.

A field seismic record is conventionally regarded as an approximation of the convolution between the reflectivity series and the seismic wavelet. Consequently, the recorded seismic spectrum inherently encodes the spectral characteristics of both the reflectivity and the source wavelet. Spectral balancing facilitates the extraction of intrinsic reflectivity information from the seismic spectrum by mitigating the influence of wavelet overprinting, thereby ensuring the fidelity of the dispersion

attribute inversion. Accordingly, the time-frequency spectrum $S(t,f)$ at each frequency must be normalized based on the peak amplitude observed near the elastic interface at the reference frequency, as formulated below:

$$\overline{S}(t,f) = S(t,f)W(f) \tag{16}$$

where $\overline{S}(t,f)$ signifies the balanced spectrum following the elimination of wavelet overprinting and $W(f)$ denotes the spectral balancing coefficient. Notably, to achieve complete removal of wavelet overprinting effects, the spectral balancing coefficients must be calculated using amplitudes from an elastic interface; this is because such interfaces are characterized by a lack of dispersion, and their spectra should theoretically remain invariant across frequencies. Consequently, $W(f)$ is computed using the following formulation:

$$W(f) = \frac{\underset{T_e}{MAX}\left[S\left(f_{ref}\right)\right]}{\underset{T_e}{MAX}[S(f)]} \tag{17}$$

where T_e represents the time interval corresponding to an elastic interface.

By substituting the balanced spectral difference vector $\begin{bmatrix} \overline{S}(t,f_1) - \overline{S}(t,f_0) \\ \overline{S}(t,f_2) - \overline{S}(t,f_0) \\ \vdots \\ \overline{S}(t,f_m) - \overline{S}(t,f_0) \end{bmatrix}$ with the corresponding reflectivity difference vector $\begin{bmatrix} R_{PP}(t,f_1) - R_{PP}(t,f_0) \\ R_{PP}(t,f_2) - R_{PP}(t,f_0) \\ \vdots \\ R_{PP}(t,f_m) - R_{PP}(t,f_0) \end{bmatrix}$, the dispersion attributes of the field seismic data can be derived based on Eq. (16).

4. Results

4.1. Rock physics modeling

Based on core interpretation results, the target sandstone aquifer is characterized by a dense lithology and the development of high-angle to vertical closed fractures and microcracks, which is consistent with the fundamental assumptions of a horizontally transverse isotropic (HTI) medium and Chapman multiscale fracture theory. Therefore, a rock physics model for the roof sandstone was constructed by integrating effective medium theory with the Chapman model.

Specifically, the primary mineral components of the sandstone were identified based on X-ray Diffraction (XRD) measurement results, as presented in Table 1. Based on these compositions, the effective bulk and shear moduli of the matrix were estimated using the Voigt-Reuss-Hill (VRH) average model. The application of the VRH model is particularly suitable for the Carboniferous-Permian strata in the study area. Due to intensive diagenetic compaction and cementation, the elastic moduli of the clay minerals have been significantly enhanced, becoming comparable to those of quartz and feldspar. This reduced contrast between mineral moduli leads to a narrowing of the gap between the Voigt (upper) and Reuss (lower) bounds. Consequently, the VRH average serves as a robust and high-precision approximation for the effective elastic properties of the sandstone matrix in this geological setting (Mondol et al., 2007). Subsequently; the moduli and viscosities of the fluid mixtures were determined using the Batzle-Wang and Wood formulations(Wood and Lindsay, 1956; Batzle and Wang, 1992). Finally, the Chapman model was utilized to incorporate pores, fractures, microcracks, and fluids into the rock matrix. Experimental and logging data indicated that the total porosity of the roof sandstone ranged from 0.04 to 0.09 with a mean value of 0.07. Therefore, the total porosity was set to 0.07 for the modeling. Given that fracture parameters are challenging to measure directly, theoretical values were adopted in this study. Following the findings of She et al. (2024) on the relaxation time in the sandstone aquifers, the τ_m for fully water-saturated and fully gas-saturated sandstones were assigned as 2×10^{-5} s and 4×10^{-7} s, respectively. For a fixed rock skeleton, the relaxation time parameter depends solely on the viscosity of the fluid mixture and is given by Eq. (2). The input parameters for the Chapman model were finalized, as summarized in Table 2, where the matrix bulk modulus was determined via the Voigt-Reuss-Hill (VRH) average of the mineral components listed in Table 1.

Fig. 3 illustrates the frequency-dependent characteristics of P-wave velocity (V_p) and the inverse quality factor ($1/Q$) under varying water saturation conditions, where S_w ranges from 0 to 1. As shown in Fig. 3a, V_p exhibited significant dispersion across the frequency range from 10^0 to 10^6 Hz for all saturation levels. At a constant frequency, V_p increased with increasing water saturation, such that the maximum velocity occurred at full saturation, while the minimum was observed in the air saturated state. This phenomenon indicates that the presence of fluids significantly enhances the equivalent bulk modulus of the medium. Notably, as S_w increased, the characteristic frequency at which V_p dispersion initiated shifted globally toward the low-frequency range, suggesting that seismic dispersion and attenuation can be triggered within seismic frequency bands under high-saturation conditions. Fig. 3b shows that, under different water saturation conditions, $1/Q$ exhibits two pronounced attenuation peaks, indicating energy dissipation induced by dual-scale fluid flow associated with the fracture system. The peak amplitudes of $1/Q$ are highly sensitive to variations in water saturation. At low frequencies, attenuation remains weak owing to fully equilibrated fluid pressure, whereas with increasing frequency, fracture-related fluid flow is progressively activated, leading to a rapid increase in $1/Q$ and the development of attenuation peaks in the intermediate-to-high frequency range.

Given that the Chapman model is governed by multiple parameters, a Sobol global sensitivity analysis was conducted to identify the dominant controls on the P-wave velocity and inverse quality factor(Sobol", 2001; Saltelli, 2002; Ba et al., 2025). Five key parameters, including water saturation, microcrack density, fracture density, fracture length, and porosity, were considered, and their respective contributions to the model uncertainty were quantified. The parameter ranges are listed in Table 3.

The Sobol global sensitivity analysis is based on the variance

Table 1
Physical property parameters of sandstone components(Mavko et al., 2020).

Properties	Content (%)	Bulk modulus (GPa)	Shear modulus (GPa)	Density(g/cm^3)
Quartz	60.1	37.0	44	2.65
Feldspar	20.8	37.5	15	2.62
Clay	19.1	21.0	7	2.60

Table 2
Input parameters for the Chapman model.

Parameters	Value	Unit
Matrix bulk modulus(K_0)	33.2	GPa
Matrix shear modulus(μ_0)	24.6	GPa
Matrix density(ρ_0)	2.63	g/cm^3
Total porosity(ϕ_p)	0.07	/
Microcrack density(ε_c)	0.05	/
Fracture density(ε_f)	0.05	/
Fracture length(ε_c)	0.10	m
Microcrack aspect ratio(r_c)	2×10^{-4}	/
Fracture aspect ratio(r_f)	2×10^{-4}	/
Grain size(ς)	5×10^{-4}	m
Brine salinity(S)	10	g/L
Brine viscosity(η_w)	6.6×10^{-4}	Pa·s
Brine bulk modulus(K_w)	2.20	GPa
Gas(Air) viscosity(η_g)	2×10^{-5}	Pa·s
Gas(Air) bulk modulus(K_g)	0.03	GPa

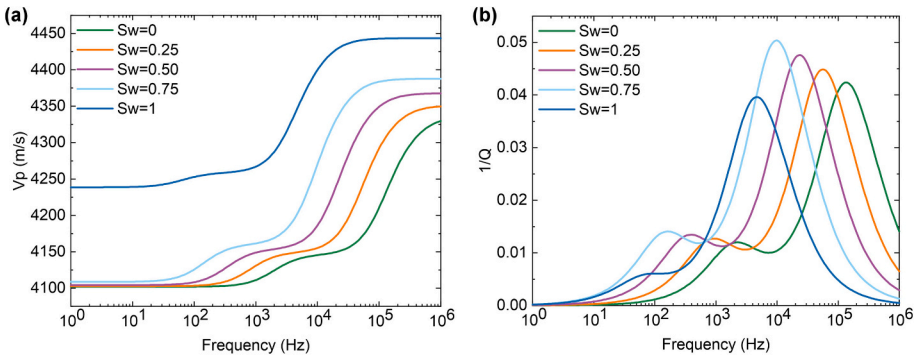

Fig. 3. Frequency-dependent P-wave velocities and inverse quality factor for various water saturation levels (a) P-wave velocity. (b) Inverse quality factor.

Table 3
Ranges in the sensitivity analysis.

Parameters	Range	Unit
Water saturation(S_w)	0–1	/
Microcrack density(ε_c)	0–0.1	/
Fracture density(ε_f)	0–0.1	/
Fracture length(a_f)	0.1–1	m
Total porosity(ϕ_p)	0.05–0.15	/

decomposition of the model output, in which the total variance is expressed as the sum of the partial variances associated with the individual input parameters and their interactions. This framework enables a quantitative evaluation of the contribution of each input parameter to the model output uncertainty. Accordingly, the first-order (S_i) and total-order (S_{Ti}) Sobol sensitivity indices were computed for all input parameters in this study.

S_i measures the fraction of the Chapman model output variance that is attributable solely to individual parameters. Higher S_i values indicate greater dominance of the parameter on the model response. S_i is computed as follows:

$$S_i = \frac{\mathrm{Var}_{X_i}\left(\mathbb{E}_{X_{\sim i}}[Y|X_i]\right)}{\mathrm{Var}(Y)} \tag{18}$$

The total-order sensitivity index (S_{Ti}) encompasses both the main effect of a parameter and all higher-order interaction effects with other parameters, reflecting its overall influence on the model output. S_{Ti} is calculated as follows:

$$S_{T_i} = 1 - \frac{\mathrm{Var}_{X_{\sim i}}\left(\mathbb{E}_{X_i}[Y|X_{\sim i}]\right)}{\mathrm{Var}(Y)} \tag{19}$$

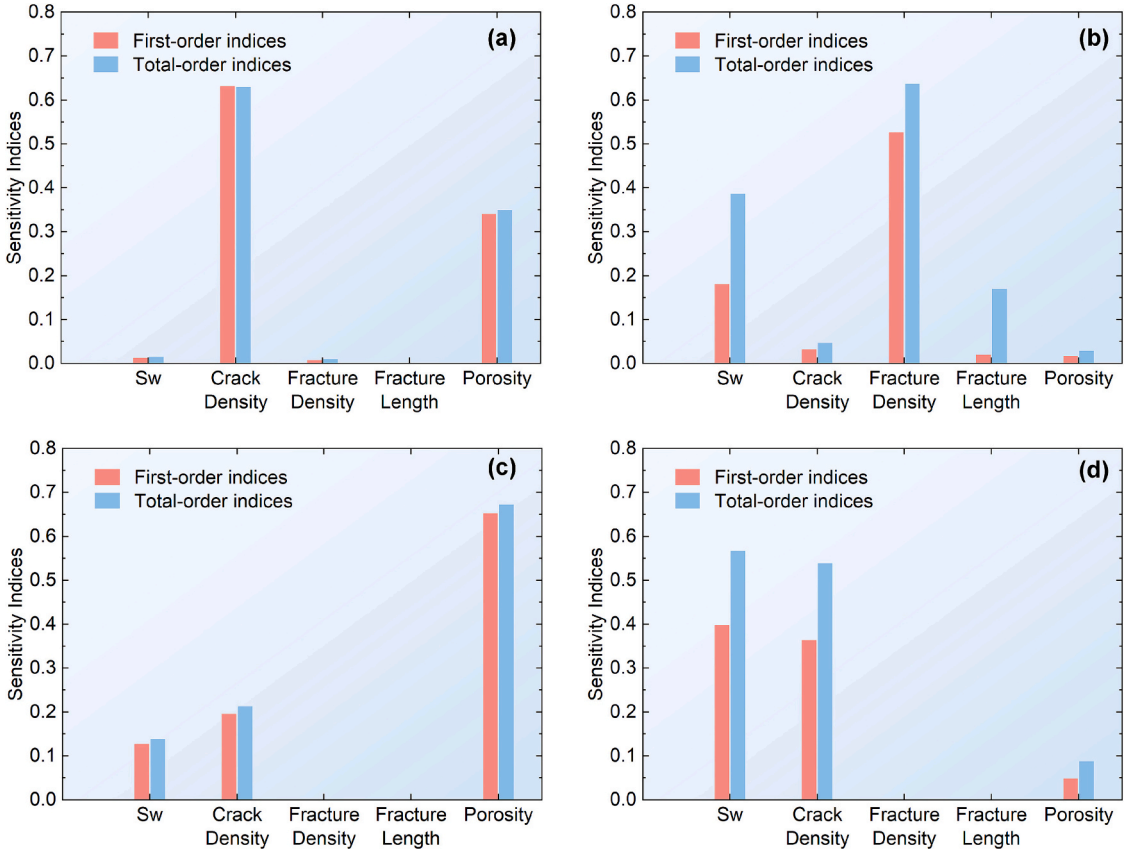

Fig. 4. The effect of water saturation, microcrack density, fracture density, fracture length, and porosity on the Chapman model results. The P-wave velocity(a) and inverse quality factor (b) of 45 Hz, respectively, and P-wave velocity(c) and inverse quality factor (d) of 0.1 MHz, respectively.

where X_i denotes the i-th input parameter, $\boldsymbol{X}_{\sim i}$ represents the set of all input parameters except X_i, $\mathbb{E}_{X_{\sim i}}[\cdot|X_i]$ represents the mean model response obtained by averaging over all parameters except X_i, while $\mathbb{E}_{X_i}[\cdot|X_{\sim i}]$ denotes the conditional expectation with respect to X_i. $\mathrm{Var}_{X_i}(\cdot)$ and $\mathrm{Var}_{X_{\sim i}}(\cdot)$ indicate the variance taken with respect to X_i and $\mathbf{X}_{\sim i}$, respectively.

Notably, given the pronounced nonlinearity of the Chapman model, sensitivity indices were computed by a Monte Carlo simulation using the Saltelli sampling strategy. A total of 2×10^6 simulations were performed to ensure statistically robust and reliable results.

Fig. 4 illustrates the Sobol sensitivity indices of V_p and $1/Q$ relative to various parameters in the Chapman model at seismic (45 Hz) and ultrasonic (0.1 MHz) frequencies. The results reveal significant differences in parameter sensitivity between V_P and $1/Q$, exhibiting pronounced frequency dependence.

For V_P, both the first- and total-order sensitivity indices of porosity are high under 45 Hz and 0.1 MHz conditions, indicating that the P-wave velocity is primarily controlled by the elastic properties of the rock matrix. Its variations are dominated by the first-order effect of porosity, with relatively weak parameter interactions. At low frequencies, the Chapman model follows Gassmann theory, and the extremely low stiffness of microcracks induces substantial perturbations to the rock's elastic properties, making V_P highly sensitive to microcrack density. At high frequencies, fluids in microcracks behave nearly incompressibly, effectively stiffening the cracks and reducing their contribution to bulk deformation, resulting in a marked decrease in V_P sensitivity to microcrack density. In contrast, water saturation exhibits a relatively minor influence on V_P, suggesting that fluid parameters play a subordinate role in P-wave response. Conversely, $1/Q$ shows pronounced sensitivity to fracture density, microcrack density, and water saturation. At low frequencies, the sensitivities of fracture density and water saturation dominate, indicating that fracture-induced patchy saturation effects govern attenuation. Within the ultrasonic frequency regime, the local pressure gradients between microcracks and pores are significantly intensified, thereby enhancing the sensitivity of $1/Q$ to water saturation and microcrack density. This phenomenon underscores the pivotal role of microcrack-induced squirt-flow mechanisms in governing energy dissipation at these high frequencies(Tisato and Madonna, 2012; Tisato and Quintal, 2013; Tisato et al., 2021).

4.2. Numerical test

To evaluate the feasibility of predicting water abundance in sandstone aquifers using dispersion attributes, a horizontally layered forward model was constructed based on the actual wireline log interpreted geological conditions, as illustrated in Fig. 5. Layers 1, 3, and 4 are elastic media, with their respective parameters provided in Table 4.

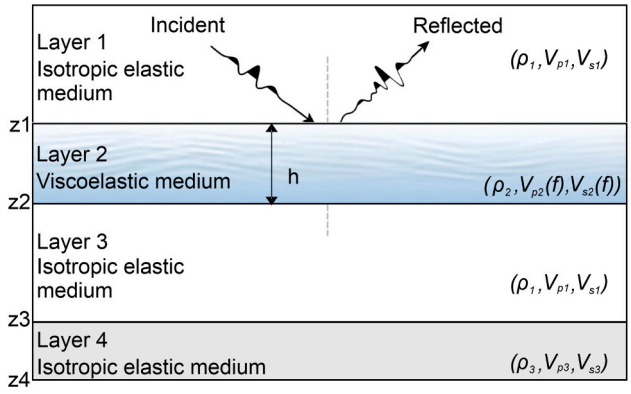

Fig. 5. Schematic diagram of the four-layer geological model used for seismic forward simulation.

Table 4
Physical parameters of the four-layer geological model for seismic forward simulation.

Layers	Density(g/cm^3)	Vp(m/s)	Vs(m/s)	Thickness
Layer 1	2.25	3000	1750	100
Layer 3	2.25	3000	1750	100
Layer 4	2.5	4000	2150	50

Layer 2, however, is a viscoelastic layer described by the Chapman model, with parameters taken directly from Table 2. The thickness of Layer 2 was fixed at 25 m, and the water saturation was systematically varied from 0 to 1.

Using the seismic forward modeling approach described in section 3.2, the intermediate layer was assigned a water saturation of 1. The variation of reflection coefficients at the medium's top interface with incidence angle and frequency is shown in Fig. 6. Across the full frequency band, the reflection coefficients exhibit periodic variations. In terms of incidence angle, the reflection coefficients vary relatively smoothly and decrease with increasing angle, consistent with the definition of Class I AVO and in agreement with the model setup.

To analyze the frequency-dependent response characteristics of realistic seismic records, a Ricker wavelet with a dominant frequency of 45 Hz was selected to synthesize seismic traces, consistent with wavelet characteristics of observed field seismic data in the study area. Under normal incidence, synthetic seismic records corresponding to sandstone layers with water saturation levels of 0, 0.4, and 0.8 are shown in Fig. 7a. As illustrated, variations in water saturation do not lead to pronounced changes in reflection waveforms or amplitudes, indicating that it is difficult to identify sandstone water abundance using conventional seismic records alone. Fig. 7b–d present the SPWVD spectral decomposition results for sandstone layers with water saturation values of 0, 0.4, and 0.8, respectively. In contrast, the time–frequency spectra reveal substantial differences across varying water saturation conditions.

To examine the influence of the seismic wavelet on the reflection spectra, the original spectral curves at 30, 40, 50, and 60 Hz were extracted for the fully water-saturated viscoelastic layer, as shown in Fig. 8a. It is evident that the elastic layers exhibit pronounced spectral discrepancies, which arise from the combined effects of reflection coefficients and wavelet energy, leading to distortion in the seismic frequency spectra. To mitigate the wavelet influence, spectral balancing was applied to the synthetic seismic records using 45 Hz as the reference frequency, following the formulation in Eqs. (18) and (19). As illustrated in Fig. 8b, after spectral balancing, the spectral amplitudes of the elastic layers become consistent across different frequency components, whereas distinct spectral differences persist within the viscoelastic layer. This indicates that dispersion-related anomalies are effectively separated from wavelet interference, and spectral balancing substantially enhances the reliability of dispersion attribute inversion.

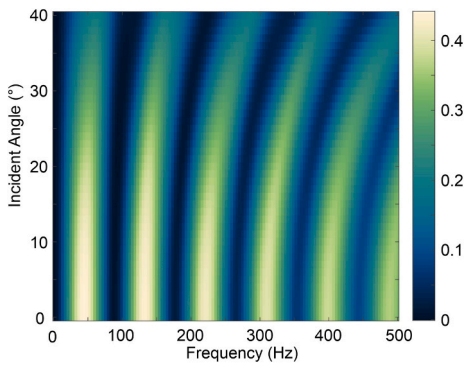

Fig. 6. Variation of reflection coefficients of the fully water-saturated viscoelastic layer with frequency and incidence angle.

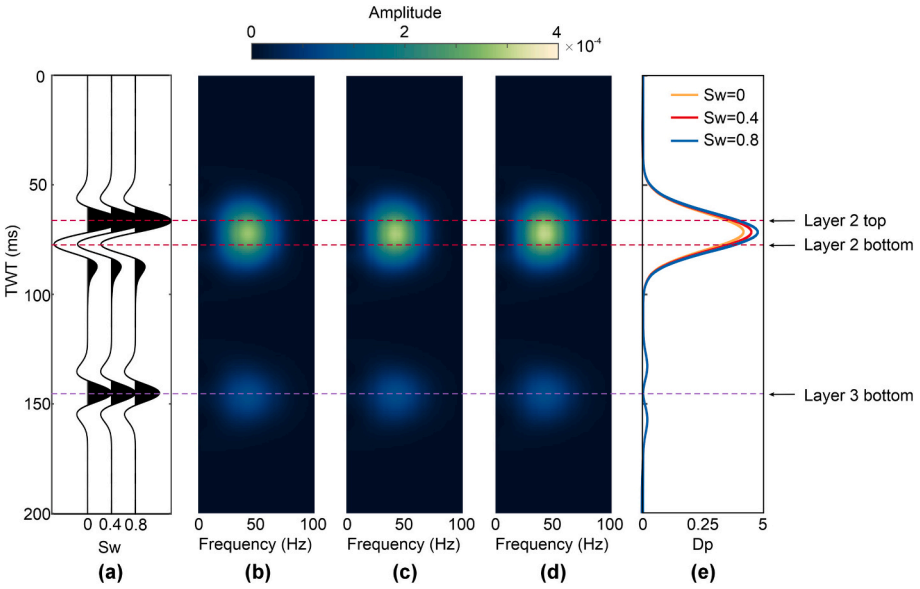

Fig. 7. Synthetic seismic records under different water saturations (a), corresponding time–frequency representations for $S_w = 0$ (b), $S_w = 0.4$ (c), and $S_w = 0.8$ (d), and the inverted dispersion attribute(e).

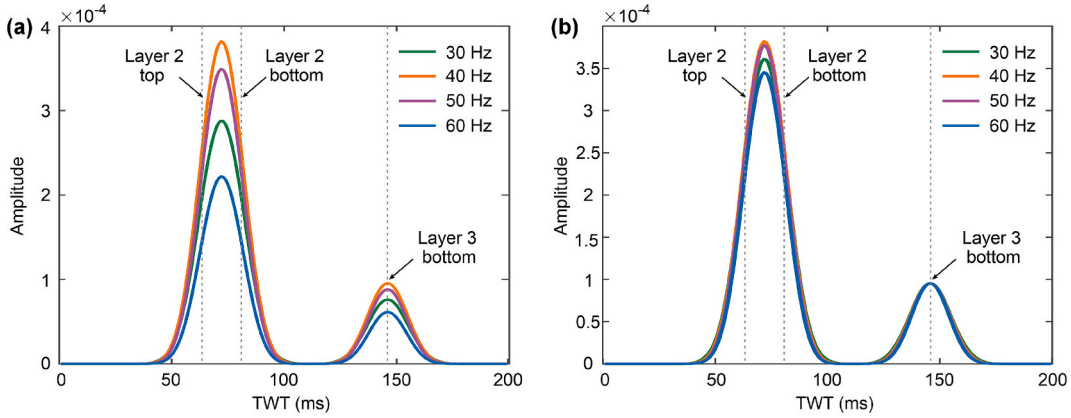

Fig. 8. Spectra of the seismic records at different frequencies (a) before and (b) after the spectrum balance.

Conventional dispersion-attribute inversion methods violate the fundamental assumptions underlying the Taylor series expansion. Therefore, the frequency-scanning approach proposed by Li et al. (2024) was adopted to invert the dispersion attribute D_p. Specifically, frequency bands within the range of 30–70 Hz were selected as reference frequencies. For each reference frequency, D_p was inverted within a narrow frequency window of 10 Hz centered on the reference frequency, and the maximum D_p value was ultimately taken as the final result. Fig. 7e shows the dispersion attributes obtained using the above inversion strategy. At the elastic layer 3 bottom (indicated by the purple dashed line), D_p is zero, whereas pronounced differences in D_p are observed near the viscoelastic layer 2 (indicated by the red dashed line) for seismic records corresponding to different water saturations. These results demonstrate the feasibility of using dispersion-attribute inversion to estimate water saturation.

To further clarify the relationship between S_w and D_p, dispersion attributes at the viscoelastic interface were inverted for different water saturations. Fig. 9 illustrates the variation of D_p with S_w at the viscoelastic layer's top interface under normal incidence. Overall, D_p exhibits a pronounced positive correlation with increasing water saturation. As S_w increases from 0 to 0.9, D_p is monotonically increasing over its domain. In contrast, at high saturations ($S_w = 0.9$–1.0), D_p shows a slight

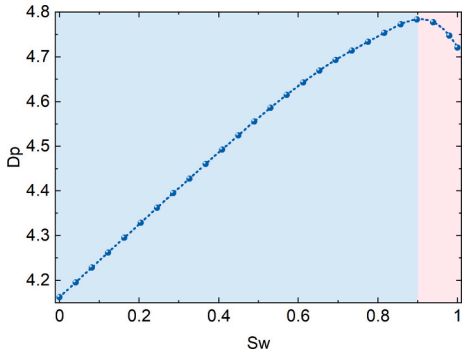

Fig. 9. Relationship between water saturation and dispersion attribute (D_p).

decrease. This behavior can be explained by the physics of wave-induced fluid flow since as the fracture and pore space become nearly fully saturated, the fluid distribution becomes more homogeneous, and the compressibility contrast diminishes, reducing the driving force for pressure relaxation and thereby weakening dispersion effects (Müller et al., 2010; Pang et al., 2019).

4.3. Case study

The No. 4 coal seam is the primary mining coal in the Hengyuan Coal Mine of the Huaibei Coalfield. The water-bearing sandstone layer in the roof poses a serious threat to its safe mining operations. Therefore, this sandstone aquifer was selected as a representative example for the case study in this work. Fig. 10 shows the wireline logs of Borehole B1 in the study area. A pronounced negative anomaly is observed in the spontaneous potential (SP) log within the yellow-highlighted interval, accompanied by a distinctly low gamma-ray response, jointly indicating the presence of a water-bearing sandstone aquifer.

The dispersion-attribute inversion in this study was performed using post-stack seismic data, which satisfy the assumptions of Eq. (11). Fig. 11a shows the post-stack seismic section crossing boreholes B1, B2, B3, and B4. Based on well-logging data and seismic traces adjacent to the boreholes, synthetic seismograms were constructed to identify the horizons of the water-bearing sandstone aquifer and the No. 4 coal seam, with the interpreted results indicated by arrows. Fig. 11b presents the amplitude spectra of the post-stack seismic data in the study area. The seismic energy is primarily concentrated in the 20–90 Hz frequency range (the light-blue region in the figure), with a dominant frequency of approximately 45 Hz. SPWVD was adopted in this case study to perform time–frequency analysis of the seismic signals, yielding spectral information over the frequency range of 20–90 Hz. The No. 4 coal seam in the region is dry and lacks fluid-related dispersion. Since coal seams are generally considered effective aquicludes with minimal dispersion effects, it was therefore selected as the elastic reference layer for spectral balancing. Fig. 12 illustrates the spectral decomposed seismic sections at 30, 40, 50, and 60 Hz before and after spectral balancing. The results indicate that, in the vicinity of the target layer, the seismic energy in different frequency bands is effectively equalized to the same order of magnitude, preventing the dispersion attribute inversion from being biased by the wavelet energy distribution and thereby providing a reliable basis for the subsequent inversion.

Subsequently, reference frequencies were scanned within the 30–70 Hz range. For each reference frequency, dispersion attributes were inverted within a narrow 10 Hz frequency window centered on the reference frequency, and the maximum inverted dispersion value was selected as the final result. The resulting dispersion-attribute section is shown in Fig. 13. Within the target sandstone layer, the intensity of D_p exhibits pronounced lateral heterogeneity and shows a clear positive correlation with the mean water saturation values at the borehole locations. Specifically, strong dispersion responses are observed in the vicinity of Boreholes B4 (S_w = 0.82) and B1 (S_w = 0.76), which are characterized by relatively high water saturation. Moderate dispersion intensity corresponds to the area around Borehole B3 (S_w = 0.68), whereas the region near Borehole B2 (S_w = 0.53) is associated with weak dispersion responses. The positive correlation between borehole-derived S_w and the intensity of D_p is consistent with the theoretical results of forward modeling, thereby providing field validation that confirms the effectiveness of dispersion attributes in identifying reservoir fluid properties.

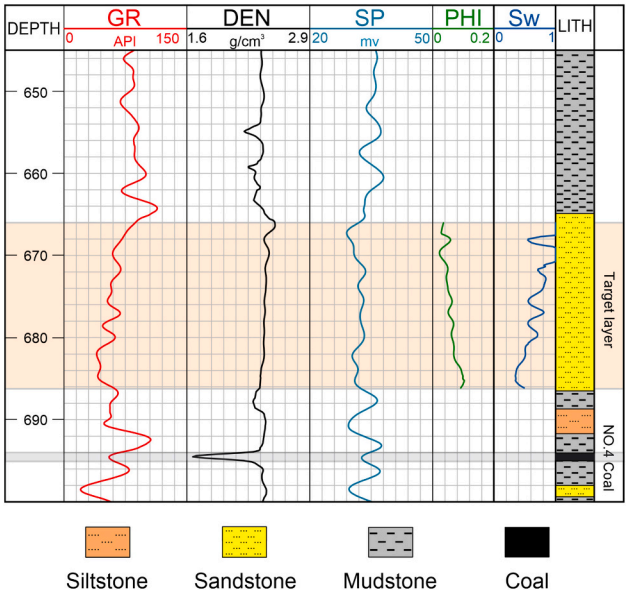

Fig. 10. The logging curves of Borehole B1.

Dispersion attributes were extracted for the target sandstone layer across the study area, and the mean dispersion value within the target interval was calculated. Fig. 14 illustrates the planar distributions of the dispersion attribute and the Root Mean Square (RMS) amplitude attribute for the target sandstone layer, with the locations of hydrogeological boreholes H1–H3 marked. Overall, D_p exhibits pronounced lateral heterogeneity throughout the study area and shows a clear positive correlation with the measured water inflow rates. Specifically, borehole H1, with a water inflow rate of 50.8 m^3/h, corresponds to a high D_p anomaly. Borehole H3, with a water inflow rate of 15.4 m^3/h, is located near a transitional zone of moderate D_p values, whereas borehole H2, which yields only 6.7 m^3/h, coincides with a distinct low D_p region. Compared with the RMS amplitude, which is primarily governed by lithology, porosity, bed-thickness tuning, and reflection interface strength and thus reflects mixed geometric and elastic effects rather than fluid-related variations, the dispersion attribute effectively captures fluid-induced frequency-dependent seismic responses, with high-value anomalies directly reflecting high water abundance predictions, thereby providing a more robust indicator of sandstone water abundance.

5. Discussion

5.1. Validation and applicability analysis

To further validate the relationship between dispersion attributes and the water inflow rates measured at hydrogeological boreholes, dispersion attribute values at hydrogeological boreholes H1, H2, and H3 were extracted, as shown in Fig. 15. *Overall, a strong positive correlation is observed between the dispersion attribute and the water inflow rate, indicating that dispersion attributes provide a robust indicator for assessing water abundance in sandstone aquifers. The technical workflow proposed in this study effectively characterizes the frequency-dependent seismic response of viscoelastic layers, thereby enabling reliable evaluation of water abundance in sandstone aquifers.*

At the same time, this study also highlights that characterizing water abundance in sandstone aquifers using frequency-dependent seismic responses remains highly challenging. As observed in the numerical tests, the Sobol sensitivity analysis of the Chapman model indicates that, within the seismic frequency band, fracture density exerts considerable control over seismic dispersion in addition to water saturation. In the present study area, faults are relatively small in scale (Fig. 1c), and no major geological structures or anomalous bodies are developed. Consequently, the spatial variations in fracture density and fracture scale are limited, and the influence of fracture-related parameters on dispersion attributes can be reasonably neglected. However, in areas characterized by intense structural deformation and heterogeneous fracture development, the capability of dispersion attributes to indicate water yield may be significantly weakened. Therefore, when applying this method in structurally complex mines, it is necessary to introduce decoupling strategies between water saturation and fracture parameters, or to establish a multi-parameter joint inversion framework, so as to effectively suppress fracture-induced effects and extract dispersion information that is more directly related to fluid properties.

Furthermore, the frequency-dependent seismic response of viscoelastic layers is influenced by multiple factors. Ouyang et al. (2023)

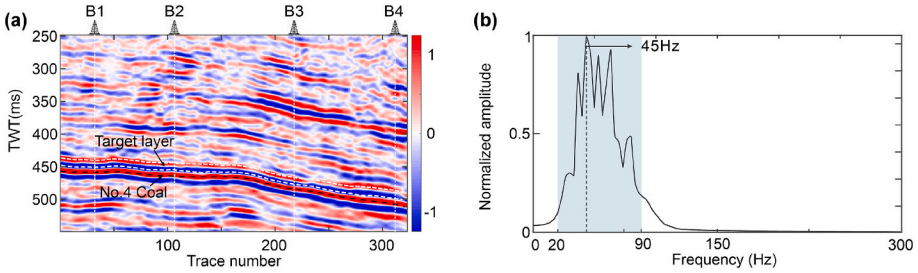

Fig. 11. Post-stack seismic section across the boreholes B1, B2, B3, and B4. (a) and corresponding amplitude spectra (b).

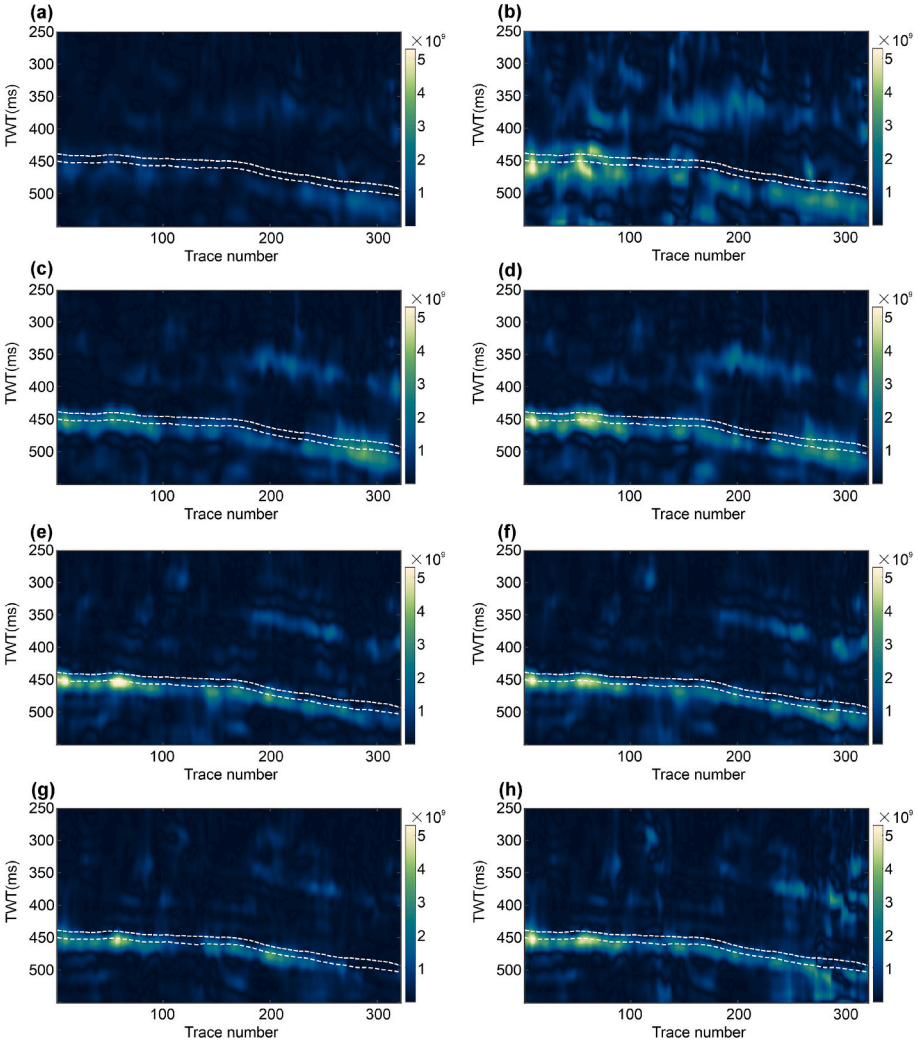

Fig. 12. Spectral decomposition sections at 30, 40, 50, and 60 Hz. (a, c, e, g) Sections before spectral balancing; (b, d, f, h) Corresponding sections after spectral balancing.

indicates that, in areas where the target layer exhibits significant thickness variations, tuning effects can substantially affect the frequency response of seismic data, which may lead to distortion in the derived dispersion attributes. In addition, seismic signal diffraction or interference near fault structures and other geological anomalies may reduce the reliability of dispersion inversion results. Moreover, the selection of the No. 4 coal seam as the elastic reference for spectral balancing is specifically optimized for this local geological setting, owing to its stable aquiclude properties and lack of fluid-induced frequency dispersion. Therefore, we strongly recommend conducting targeted regional geological analyses and forward-modeling simulations when applying this method to other study areas.

5.2. *Impact of seismic SNR on dispersion attribute inversion*

The quality of seismic data directly determines the reliability of dispersion-attribute inversion. To quantitatively assess the impact of seismic signal-to-noise ratio (SNR) on inversion accuracy, different levels of Gaussian random noise were added to the original synthetic seismic records, generating records with SNRs of 25 dB, 20 dB, 15 dB, and 10 dB (Fig. 16). As illustrated, with increasing noise levels, the continuity of seismic events along the in-phase axis gradually

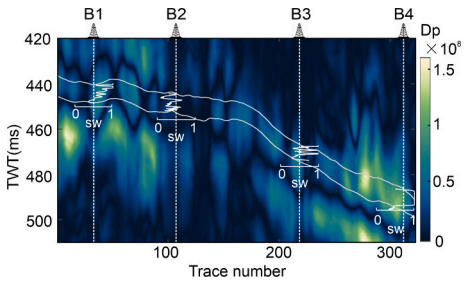

Fig. 13. Section of the inverted dispersion attribute (D_p) across the boreholes B1, B2, B3, and B4.

deteriorates, and the effective signal is increasingly obscured by ambient noise, resulting in a significant decline in seismic data quality.

The dispersion-attribute inversion results (Fig. 17) indicate that noise exerts a significant influence on the inversion process. When SNR $>$ 20 dB, the inversion exhibits good robustness: the D_p response is clear, and the curve shapes are well-preserved. However, as SNR decreases further (SNR $<$ 15 dB), the inversion results become markedly unstable. Specifically, at the elastic interface (purple dashed line), the inverted dispersion attribute remains zero, reflecting the method's stability in elastic layers. In contrast, at the dispersive interface (red dashed line), the inversion results are highly sensitive to noise: the fluctuations in D_p values become increasingly severe, and the peak shapes of the inversion curves are distorted. Under extreme conditions (SNR = 10 dB), the positive correlation between dispersion attribute and water saturation is significantly disrupted. These results indicate that, for real datasets, low-SNR seismic data can only provide qualitative identification of water-bearing layers and are insufficient for quantitative assessment of water abundance. To ensure reliable predictions of water abundance, seismic data with the highest possible SNR should be selected.

5.3. Implications for CO_2 sequestration

In the site selection of geological CO_2 storage (CCS) projects, deep saline aquifers are considered ideal carbon storage targets due to their wide distribution and large storage potential. The quantitative evaluation method for sandstone water abundance established in this study, based on dispersion attributes, is not only applicable to hydrogeological investigations but also provides a valuable reference for detailed characterization of potential CO_2 storage sites. This approach can effectively identify fluid-rich zones with high porosity and connectivity necessary for supercritical CO_2 injection, offering a scientific basis for early-stage site evaluation. Furthermore, the injection of CO_2 into saline aquifers establishes a sophisticated CO_2–brine–rock system that develops within the saline aquifer, inevitably giving rise to intricate dispersion and dissipation mechanisms. The analysis of frequency-dependent seismic responses of sandstone under varying fluid saturation conditions, as presented in this study, facilitates the construction of more reliable rock

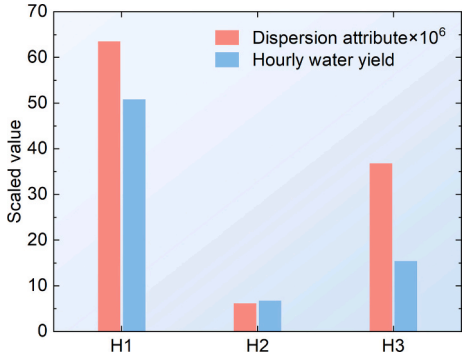

Fig. 15. Hourly water yield at hydrogeological boreholes and the corresponding dispersion attributes.

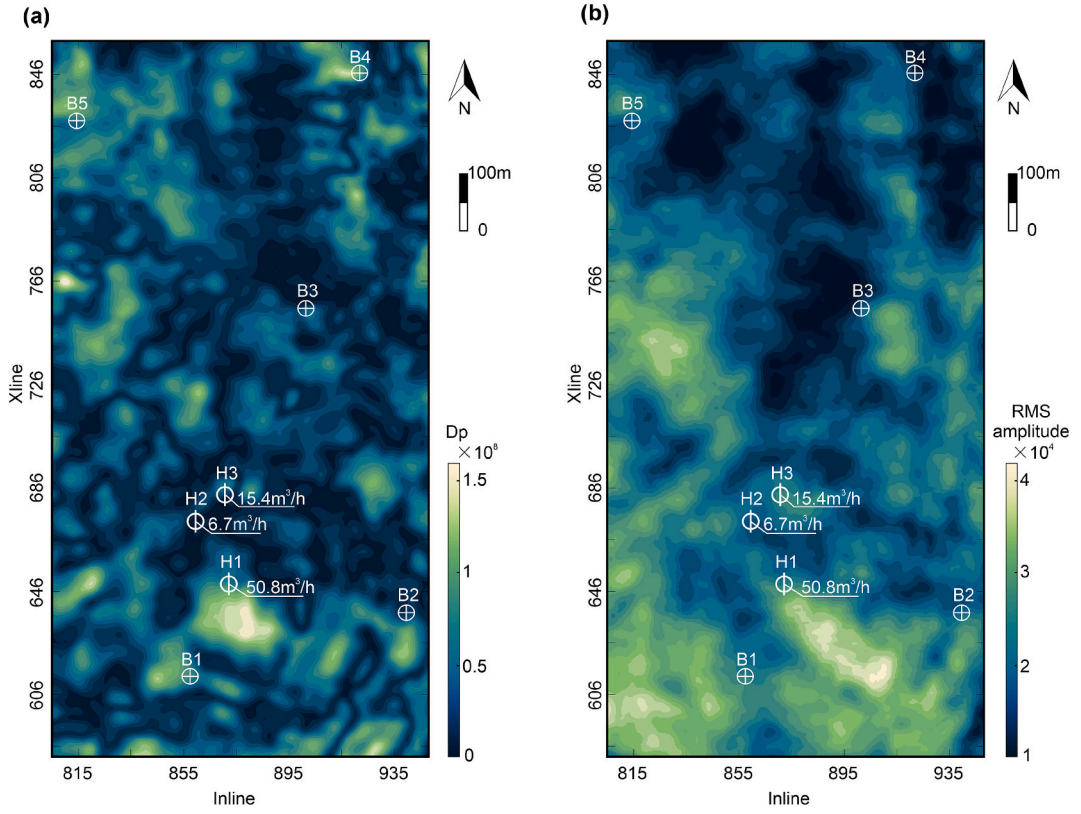

Fig. 14. Distribution of (a) the dispersion attribute and (b) the Root Mean Square (RMS) amplitude for the sandstone aquifer.

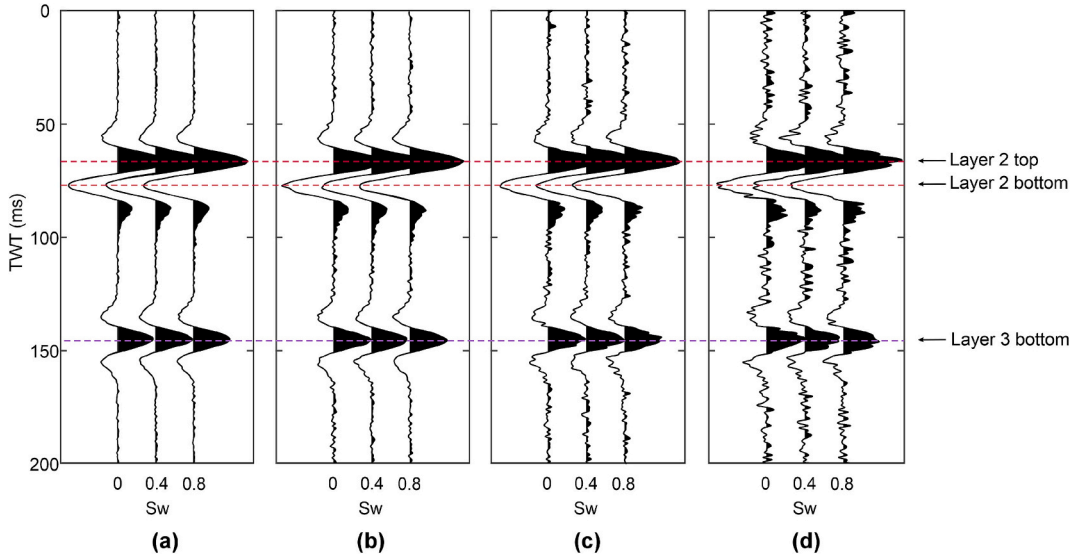

Fig. 16. Synthetic seismic records with signal-to-noise ratios of 25 dB (a), 20 dB (b), 15 dB(c), and 10 dB (d).

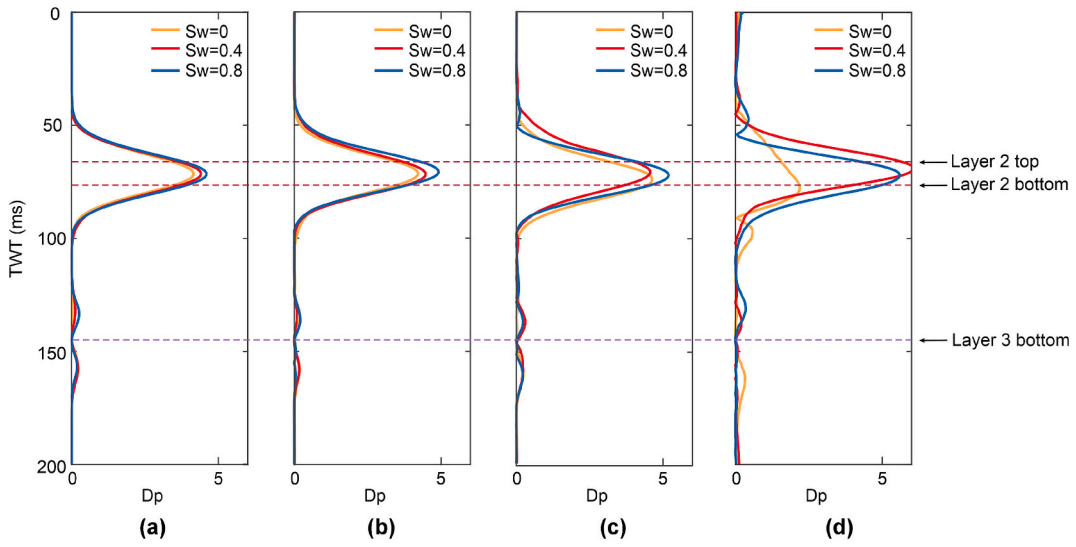

Fig. 17. Dispersion attribute inversion results from synthetic seismic records with signal-to-noise ratios of 25 dB (a), 20 dB (b), 15 dB(c), and 10 dB (d).

physics models for deep saline formations. Moreover, following CO_2 injection, the reservoir fluid saturation evolves from pure brine to a CO_2–brine mixture, which substantially alters the intensity of dispersion attributes. By monitoring the spatiotemporal evolution of dispersion attributes, the migration of CO_2 plumes can be quantitatively assessed. In conclusion, this study contributes not only to static site evaluation but also provides a critical rock physics reference for assessing reservoir integrity during the long-term monitoring of CCS projects. These findings are instrumental in identifying carbon storage spaces and ensuring the long-term feasibility as well as operational safety of carbon sequestration initiatives.

6. Conclusion

A quantitative workflow integrating frequency-dependent rock physics modeling, seismic forward simulation, and dispersion-attribute inversion is established for evaluating the water abundance of roof sandstone aquifers. A frequency-dependent rock-physics model for water-bearing sandstone is constructed by coupling effective medium theory with Chapman's multiscale fracture model, providing a physical basis for describing fluid-induced dispersion and attenuation in fractured sandstone. Sobol global sensitivity analysis of the rock-physics model indicates that, within the seismic frequency band, P-wave velocity is primarily controlled by porosity, whereas the inverse quality factor is mainly sensi tive to water saturation and fracture density. Based on the established rock-physics model, seismic forward modeling is performed using the propagator matrix method to simulate reflection responses of viscoelastic layered media under different water saturation conditions. A positive relationship between dispersion attributes and water saturation is revealed, clarifying the theoretical link between seismic dispersion and aquifer water saturation. In the field application, post-stack seismic data were analyzed using the smoothed pseudo Wigner–Ville distribution combined with spectral balancing to obtain high-resolution time–frequency spectra. Dispersion attributes extracted through a frequency-scanning strategy exhibit pronounced lateral heterogeneity in the roof sandstone and show a significant positive correlation with hourly water inflow rates measured at hydrogeological boreholes. These results confirm that seismic dispersion attributes derived from stacked seismic data can be used for quantitative evaluation of sandstone aquifer water abundance. The proposed frequency-

dependent rock physics framework not only provides direct geophysical support for roof water-hazard prevention but also offers important rock physics references for site selection and performance monitoring in CO_2 geological storage, where the higher compressibility of supercritical CO_2 enhances the fluid-matrix modulus contrast compared to water, resulting in more pronounced and detectable dispersion signatures.

CRediT authorship contribution statement

Hang Yu: Writing – original draft, Visualization, Validation, Software, Methodology, Funding acquisition, Conceptualization. **Tongjun Chen:** Writing – review & editing, Supervision, Resources, Funding acquisition. **Luca de Siena:** Writing – review & editing, Supervision. **Heng Zhang:** Data curation. **Haiyang Yin:** Formal analysis. **Wan Li:** Investigation. **Haicheng Xu:** Investigation.

Declaration of competing interest

The authors declare that they have no known competing financial interests or personal relationships that could have appeared to influence the work reported in this paper.

Acknowledgements

This work was financially supported by the Deep Earth Probe and Mineral Resources Exploration-National Science and Technology Major Project (No.2024ZD1004201), the Graduate Innovation Program of China University of Mining and Technology (KYCX24_2837), the Postgraduate Research & Practice Innovation Program of Jiangsu Province (2024WLKXJ003), and the Program of China Scholarship Council (No.202506420076). Moreover, I would like to thank the reviewers and editors for their valuable comments, which improved the quality of this paper.

Appendix A. Chapman provided the expressions for the individual stiffness constants, as given in Eqs. (A-1)-(A-5)

$$\begin{aligned} C_{11} &= (\lambda+2\mu) - \varepsilon_c\left[\frac{8L_2(1-\nu)}{3\mu} + \frac{128}{45}\frac{1-\nu}{(2-\nu)}\mu\right. \\ &\left. -\frac{8L_2(1-\nu)}{\mu}G_1 - \frac{8K^2(1-\nu)}{\mu}G_2 - \frac{8\lambda K(1-\nu)}{3\mu}G_3\right] \\ &-\phi_p\left[\frac{3}{4\mu}\frac{1-\nu}{1+\nu}\times\left(3\lambda^2+4\lambda\mu+\frac{36+20\nu}{7-5\nu}\mu^2\right) - \left(1+\frac{3K}{4\mu}\right)(3KD_1+\lambda D_2)\right] \\ &-\varepsilon_f\left[\frac{8\lambda^2(1-\nu)}{3\mu} - \frac{8\lambda K(1-\nu)}{\mu}F_1 - \frac{8\lambda^2(1-\nu)}{3\mu}F_2\right]; \end{aligned} \tag{A-1}$$

$$\begin{aligned} C_{33} &= (\lambda+2\mu) - \varepsilon_c\left[\frac{8L_2(1-\nu)}{3\mu} + \frac{128}{45}\frac{1-\nu}{(2-\nu)}\mu\right. \\ &\left. -\frac{8L_2(1-\nu)}{\mu}G_1 - \frac{8K^2(1-\nu)}{\mu}G_2 - \frac{8(\lambda+2\mu)K(1-\nu)}{3\mu}G_3\right] \\ &-\phi_p\left[\frac{3}{4\mu}\frac{1-\nu}{1+\nu}\times\left(3\lambda^2+4\lambda\mu+\frac{36+20\nu}{7-5\nu}\mu^2\right) - \left(1+\frac{3K}{4\mu}\right)(3KD_1+(\lambda+2\mu)D_2)\right] \\ &-\varepsilon_f\left[\frac{8(\lambda+2\mu)^2(1-\nu)}{3\mu} - \frac{8(\lambda+2\mu)K(1-\nu)}{\mu}F_1 - \frac{8(\lambda+2\mu)^2(1-\nu)}{3\mu}F_2\right]; \end{aligned} \tag{A-2}$$

$$\begin{aligned} C_{44} &= \mu - \varepsilon_c\left[\frac{32}{45}\mu(1-\nu)(1-G_1) + \frac{32}{45}\frac{1-\nu}{2-\nu}\mu\right] \\ &-15\phi_p\frac{1-\nu}{7-5\nu}\mu - \varepsilon_f\frac{16(1-\nu)}{3(2-\nu)}\mu \end{aligned} \tag{A-3}$$

$$\begin{aligned} C_{12} &= \lambda - \varepsilon_c\left[\frac{8L_4(1-\nu)}{\mu} - \frac{64}{45}\frac{1-\nu}{2-\nu}\mu\right. \\ &\left. -\frac{8L_4(1-\nu)}{3\mu}G_1 - \frac{8K^2(1-\nu)}{3\mu}G_2 - \frac{8K(1-\nu)}{3\mu}G_3\right] \\ &-\phi_p\left[\frac{3(1-\nu)}{4\mu(1+\nu)}\left(3\lambda^2+4\lambda\mu-\frac{4(1+5\nu)}{7-5\nu}\mu^2\right) - \left(1+\frac{3K}{4\mu}\right)(3KD_1+\lambda D_2)\right] \\ &-\varepsilon_f\left[\frac{8\lambda^2(1-\nu)}{3\mu} - \frac{8\lambda K(1-\nu)}{\mu}F_1 - \frac{8\lambda^2(1-\nu)}{3\mu}F_2\right] \end{aligned} \tag{A-4}$$

$$
\begin{aligned}
C_{13} = \lambda - \varepsilon_c \Bigg[& \frac{8L_4(1-\nu)}{\mu} - \frac{64}{45}\frac{1-\nu}{2-\nu}\mu \\
& - \frac{8L_4(1-\nu)}{3\mu}G_1 - \frac{8K^2(1-\nu)}{3\mu}G_2 - \frac{8(\lambda+\mu)K(1-\nu)}{3\mu}G_3 \Bigg] \\
- \phi_p \Bigg[& \frac{3(1-\nu)}{4\mu(1+\nu)}\left(3\lambda^2 + 4\lambda\mu - \frac{4(1+5\nu)}{7-5\nu}\mu^2\right) - \left(1+\frac{3K}{4\mu}\right)(3KD_1 + (\lambda+\mu)D_2) \Bigg] \\
& - \varepsilon_f \left[\frac{8\lambda(\lambda+\mu)(1-\nu)}{3\mu} - \frac{8(\lambda+\mu)K(1-\nu)}{\mu}F_1 - \frac{8\lambda(\lambda+\mu)(1-\nu)}{3\mu}F_2 \right]
\end{aligned}
\tag{A-5}
$$

where λ and μ are the Lamé constants of the rock matrix, ν is Poisson's ratio of the rock matrix, ε_c denotes the microcrack density, ϕ_p is the porosity, and ε_f represents the mesoscopic fracture density. Parameters D_1, D_2, G_1, G_2, G_3, F_1, F_2, L_2, and L_4 are calculated using Eqs. (A-6)-(A-14).

$$
\begin{aligned}
D_1 = & \left[(1-\iota)\gamma + \frac{(1-\iota)\beta}{1+i\omega\tau_f} + \left(\iota + \frac{\iota\beta}{1+i\omega\tau_f}\right) \times \left(\frac{1+i\omega\gamma\tau_m}{1+i\omega\tau_m}\right) \right]^{-1} \\
& \times \left[\frac{\iota}{3(1+K_c)} + (1-\iota)\gamma' - \frac{i\omega\tau_m}{1+i\omega\tau_m}\left(\frac{1}{3(1+K_c)} - \gamma'\right) \times \left(\iota + \frac{\iota\beta}{1+i\omega\tau_f}\right) \right]
\end{aligned}
\tag{A-6}
$$

$$
\begin{aligned}
D_2 = & \left[(1-\iota)\gamma + \frac{(1-\iota)\beta}{1+i\omega\tau_f} + \left(\iota + \frac{\iota\beta}{1+i\omega\tau_f}\right) \times \left(\frac{1+i\omega\gamma\tau_m}{1+i\omega\tau_m}\right) \right]^{-1} \\
& \times \left(\frac{\beta}{(1+K_c)(1+i\omega\tau_f)} \right)
\end{aligned}
\tag{A-7}
$$

$$
G_1 = \frac{i\omega\tau_m}{(1+K_c)(1+i\omega\tau_m)} \tag{A-8}
$$

$$
G_2 = \frac{1+i\omega\gamma\tau_m}{1+i\omega\tau_m}D_1 - \frac{i\omega\tau_m\gamma'}{1+i\omega\tau_m} \tag{A-9}
$$

$$
G_3 = \frac{1+i\omega\gamma\tau_m}{1+i\omega\tau_m}D_2 \tag{A-10}
$$

$$
F_1 = \frac{1}{1+i\omega\tau_f}\left[\frac{1+i\omega\gamma\tau_m}{1+i\omega\tau_m}\iota D_1 + (1-\iota)D_1 + \frac{i\omega\tau_m}{1+i\omega\tau_m}\left(\frac{1}{3(1-K_c)} - \gamma'\right) \right]; \tag{A-11}
$$

$$
F_2 = \frac{1}{1+i\omega\tau_f} \times \left[\frac{i\omega\tau_f}{1+K_c} + \iota\frac{1+i\omega\gamma\tau_m}{1+i\omega\tau_m}D_2 + (1-\iota)D_2 \right] \tag{A-12}
$$

$$
L_2 = \lambda^2 + \frac{4}{3}\lambda\mu + \frac{4}{5}\mu^2 \tag{A-13}
$$

$$
L_4 = \lambda^2 + \frac{4}{3}\lambda\mu + \frac{4}{15}\mu^2 \tag{A-14}
$$

Chapman defined:

$$
\begin{cases}
\gamma = \dfrac{3\pi}{8(1-\nu)}\left(1 + \dfrac{4}{3}\dfrac{\rho_s}{\rho_f}\left(\dfrac{V_s}{V_f}\right)^2\right) \\
K_p = \dfrac{4\mu}{3K_f} \\
\gamma' = \gamma\dfrac{1-\nu}{1+\nu}\dfrac{1}{1+K_p} \\
K_c = \dfrac{\pi\mu r}{2K_f(1-\nu)}
\end{cases}
\tag{A-15}
$$

where V_s is the shear-wave velocity of the rock matrix, ρ_f is the density of the pore fluid, V_f is the P-wave velocity of the pore fluid, K_f is the bulk modulus of the pore fluid, r denotes the fracture aspect ratio, and ω is the angular frequency.

For sufficiently small aspect ratios, we takes $K_c = 0$. We introduce the further notation:

$$
\begin{cases}
l = \dfrac{4\pi\epsilon_c/3}{4\pi\epsilon_c/3 + \phi_p} \\
\beta = \dfrac{4\pi\epsilon_f/3}{4\pi\epsilon_f/3 + \phi_p}
\end{cases}
\tag{A-16}
$$

The Chapman model accounts for fluid dynamics at both microscopic and mesoscopic scales. Within this framework, the microscopic relaxation time, denoted as τ_m, typically resides within the ultrasonic frequency range. Conversely, the mesoscopic relaxation time, τ_f, generally manifests within

the seismic frequency band. These two parameters govern the specific frequency bands in which fluid dissipation occurs at different scales, and their calculation formulas are as follows:

$$\begin{cases} \tau_{\mathrm{f}} = \left(\dfrac{a_{\mathrm{f}}}{\varsigma}\right)\tau_{\mathrm{m}} \\ \tau_{\mathrm{m}} = \dfrac{c_{\mathrm{v}}\eta(1+K_{\mathrm{c}})}{\sigma_{\mathrm{c}}k\varsigma c_1} \end{cases} \tag{A-17}$$

Where a_{f} is the radius of the fractures, ς is the rock grain size, c_{v} is the volume of an individual microcrack, η is the viscosity of the pore fluid, σ_{c} is the critical stress, c_1 is the number of interconnected pores and fractures, and k is the permeability.

Appendix B. In Eq. (5), i_P is the incident vector of the P wave, expressed as

$$i_P = i\omega\left[\beta_{P_1}, \gamma_{S_1}, -Z_{P_1}, -W_{P_1}\right]^{\mathrm{T}} \tag{B-1}$$

The propagator matrix of the upper media $\mathbf{A}_1$ is given by:

$$A_1 = i\omega\begin{bmatrix} \beta_{P_1} & \beta_{S_1} & 0 & 0 \\ -\gamma_{P_1} & -\gamma_{S_1} & 0 & 0 \\ -Z_{P_1} & -Z_{S_1} & 0 & 0 \\ W_{P_1} & W_{S_1} & 0 & 0 \end{bmatrix} \tag{B-2}$$

The propagator matrix of the lower media $\mathbf{A}_2$ is given by:

$$A_2 = i\omega \times \begin{bmatrix} 0 & 0 & \beta_{P_2}e^{\left(-i\omega S_{P_2}h\right)} & \beta_{S_2}e^{\left(-i\omega S_{S_2}h\right)} \\ 0 & 0 & \gamma_{P_2}e^{\left(-i\omega S_{P_2}h\right)} & \gamma_{S_2}e^{\left(-i\omega S_{S_2}h\right)} \\ 0 & 0 & -Z_{P_2}e^{\left(-i\omega S_{P_2}h\right)} & -Z_{S_2}e^{\left(-i\omega S_{S_2}h\right)} \\ 0 & 0 & -W_{P_2}e^{\left(-i\omega S_{P_2}h\right)} & -W_{S_2}e^{\left(-i\omega S_{S_2}h\right)} \end{bmatrix} \tag{B-3}$$

The propagator matrix of the intermediate media **B** is a matrix related to the thickness h of the intermediate layer and is expressed as:

$$B = T(0)T^{-1}(h) \tag{B-4}$$

Inside the layer at depth z, **T**(z) can be written as:

$$T(z) = i\omega\begin{pmatrix} \beta_P & \beta_S & \beta_P & \beta_S \\ -\gamma_P & -\gamma_S & \gamma_P & \gamma_S \\ -Z_P & -Z_S & -Z_P & -Z_S \\ W_P & W_S & -W_P & -W_S \end{pmatrix} \times \begin{pmatrix} e^{i\omega S_P z} & 0 & 0 & 0 \\ 0 & e^{i\omega S_S z} & 0 & 0 \\ 0 & 0 & e^{-i\omega S_P z} & 0 \\ 0 & 0 & 0 & e^{-i\omega S_S z} \end{pmatrix} \tag{B-5}$$

Where i denotes the imaginary unit, ω is the angular frequency of the incident wave, and the subscripts P and S of the variables β, γ, W and Z correspond to the qP- and qS- waves, respectively. Subscripts 1 and 2 denote the upper and lower media, respectively. For simplicity, the subscripts may be omitted, and the variables can be written in abbreviated form as:

$$\beta = p.v.\left[\frac{C_{55}s^2 + C_{33}s_z^2 - \rho}{C_{11}s^2 + C_{33}s_z^2 + C_{55}\left(s_z^2 + s^2\right) - 2\rho}\right]^{1/2} \tag{B-6}$$

$$\gamma = \pm p.v.\left[\frac{C_{11}s^2 + C_{33}s_z^2 - \rho}{C_{11}s^2 + C_{33}s_z^2 + C_{55}\left(s_z^2 + s^2\right) - 2\rho}\right]^{1/2} \tag{B-7}$$

$$W = C_{55}(\gamma s + \beta s_z) \tag{B-8}$$

$$Z = \beta C_{13}s + \gamma C_{33}s_z \tag{B-9}$$

where $p.v.$ denotes the principal value of the complex quantity. For γ, the + and - signs correspond to the qP- and qS- waves, respectively. C_{11}, C_{13}, C_{33}, and C_{55} are the stiffness constants of the medium, and ρ is the density of the medium.

s denotes the horizontal slowness and is expressed as:

$$s = \frac{\sin\theta}{v_p} \tag{B-10}$$

θ is the incident angle. For anisotropic media, v_p is given by:

$$v_p = \sqrt{\frac{C_{11}\sin^2\theta + C_{33}\cos^2\theta + C_{55} + \sqrt{E}}{2\rho}} \tag{B-11}$$

$$E = \left[(C_{11} - C_{55})\sin^2\theta - (C_{33} - C_{55})\cos^2\theta\right]^2 + 4(C_{13} + C_{55})^2\sin^2\theta\cos^2\theta \tag{B-12}$$

s_z denotes the vertical slowness and is expressed as:

$$s_z = \pm\frac{1}{\sqrt{2}}\left(K_1 \mp p.v.\sqrt{K_1^2 - 4K_2K_3}\right)^{1/2} \tag{B-13}$$

where K_1, K_2 and K_3 are given by:

$$\begin{cases} K_1 = \rho\left(\frac{1}{C_{55}} + \frac{1}{C_{33}}\right) + \frac{1}{C_{55}}\left[\frac{C_{13}}{C_{33}}(C_{13} + 2C_{55}) - C_{11}\right]s^2 \\ K_2 = \frac{1}{C_{33}}\left(C_{11}s^2 - \rho\right) \\ K_3 = s^2 - \frac{\rho}{C_{55}} \end{cases} \tag{B-14}$$

In Eq. (B-13), (+,−) denotes the downward-propagating *qP*- wave, (+,+) denotes the downward-propagating *qS*- wave, (−,−) denotes the upward-propagating *qP*- wave, and (−,+) denotes the upward-propagating *qS*- wave.

Data availability

Data will be made available on request.

References

Ajaz, M., 2021. Fluid identification and effective fracture prediction based on frequency-dependent AVOAz inversion for fractured reservoirs. Pet. Sci. https://doi.org/10.1016/j.petsci.2021.07.011.

Al-Ashqar, N.A., El-Werr, A.-K., Helaly, A.S., Kamel, A., 2025. AVO reflectivity and pre-stack seismic impedance inversion for gas sand channel detection at south abu el Naga field, onshore nile delta, Egypt. Sci. Rep. 15, 20117. https://doi.org/10.1038/s41598-025-04251-6.

Allam, H., Metwally, A., Ismael, M., Chilala, G., Elkarmoty, M., Kamel, M.H., 2025. Subsurface voids detection using GPR and ERT techniques: a case study in sukari gold mine, Egypt. Pure Appl. Geophys. 182, 4137–4167. https://doi.org/10.1007/s00024-025-03805-z.

Ba, J., Xu, W., Fu, L., Carcione, J.M., Zhang, L., 2017. Rock anelasticity due to patchy saturation and fabric heterogeneity: a double double-porosity model of wave propagation. J. Geophys. Res. Solid Earth 122, 1949–1976. https://doi.org/10.1002/2016JB013882.

Ba, J., Ma, R., Carcione, J.M., Shi, Y., Zhang, L., 2023. Effects of pore geometry and saturation on the behavior of multiscale waves in tight sandstone layers. J. Geophys. Res. Solid Earth 128, e2023JB027542, 10/gtffbg.

Ba, J., Che, H., Sun, C., Zhang, L., Carcione, J.M., 2025. Modeling seismic attenuation and dispersion in partially saturated rocks based on fluid distribution from computed tomography scans. Geophysics 90, MR239–MR250. https://doi.org/10.1190/geo2024-0315.1.

Batzle, M., Wang, Z., 1992. Seismic properties of pore fluids. Geophysics 57, 1396–1408. https://doi.org/10.1190/1.1443207.

Biot, M.A., 1956. Theory of propagation of elastic waves in a fluid-saturated porous solid. II. Higher frequency range. J. Acoust. Soc. Am. 28, 179–191. https://doi.org/10.1121/1.1908241.

Carcione, J.M., 1997. Reflection and transmission of *qP-qS* plane waves at a plane boundary between viscoelastic transversely isotropic media. Geophys. J. Int. 129, 669–680. https://doi.org/10.1111/j.1365-246X.1997.tb04502.x.

Carcione, J.M., 2001. AVO effects of a hydrocarbon source-rock layer. Geophysics 66 (2), 419–427. https://doi.org/10.1190/1.1444933.

Carcione, J., 2022. Wave Fields in Real Media : Wave Propagation in Anisotropic, Anelastic, Porous and Electromagnetic Media.

Chakraborty, A., Okaya, D., 1995. Frequency-time decomposition of seismic data using wavelet-based methods. Geophysics 60, 1906–1916. https://doi.org/10.1190/1.1443922.

Chapman, M., 2003. Frequency-dependent anisotropy due to meso-scale fractures in the presence of equant porosity. Geophys. Prospect. 51, 369–379. https://doi.org/10.1046/j.1365-2478.2003.00384.x.

Chapman, M., Maultzsch, S., Liu, E., Li, X.-Y., 2003. The effect of fluid saturation in an anisotropic multi-scale equant porosity model. J. Appl. Geophys. 54, 191–202. https://doi.org/10.1016/j.jappgeo.2003.01.003.

Dong, S., Wang, H., Guo, X., Zhou, Z., 2021. Characteristics of water hazards in China's coal mines: a review. Mine Water Environ. 40, 325–333. https://doi.org/10.1007/s10230-021-00770-6.

El Hameedy, M.A., Mabrouk, W.M., Dahroug, S., Youssef, M.S., Metwally, A.M., 2023. Role of seismic refraction tomography (SRT) in bedrock mapping; case study from industrial zone, Ain-sokhna area, Egypt. Contrib. Geophys. Geod. 53, 111–128. https://doi.org/10.31577/congeo.2023.53.2.2.

Farfour, M., Castagna, J.P., 2024. A new expression for fluid factor using AVO intercept and gradient: Theory and application on gas sand reservoirs from offshore Australia. Interpretation 12, B17–B27. https://doi.org/10.1190/INT-2023-0088.1.

Fattahi, H., Karimpouli, S., 2016. Prediction of porosity and water saturation using pre-stack seismic attributes: a comparison of bayesian inversion and computational intelligence methods. Comput. Geosci. 20, 1075–1094. https://doi.org/10.1007/s10596-016-9577-0.

Fawad, M., Hansen, J.A., Mondol, N.H., 2020. Seismic-fluid detection-a review. Earth-Sci. Rev. 210, 103347. https://doi.org/10.1016/j.earscirev.2020.103347.

Guo, Z., Zhang, X., Liu, C., 2022a. An improved scheme of azimuthally anisotropic seismic inversion for fracture prediction in volcanic gas reservoirs. IEEE Trans. Geosci. Remote Sens. 60, 1–12, 10/gq4jwx.

Guo, Z., Zhao, D., Liu, C., 2022b. Gas prediction using an improved seismic dispersion attribute inversion for tight sandstone gas reservoirs in the Ordos basin. China. J. Nat. Gas Sci. Eng. 101, 104499. https://doi.org/10.1016/j.jngse.2022.104499.

Guo, Z., Zhao, D., Liu, C., 2022c. A new seismic inversion scheme using fluid dispersion attribute for direct gas identification in tight sandstone reservoirs. Remote Sens. 14, 5326. https://doi.org/10.3390/rs14215326.

Guo, Z., Zhang, T., Liu, C., 2023. Direct hydrocarbon identification in shale oil reservoirs using fluid dispersion attribute based on an extended frequency-dependent seismic inversion scheme. Pet. Sci. 20, 1532–1545. https://doi.org/10.1016/j.petsci.2022.12.011.

Hameedy, M.A.E., Mabrouk, W.M., Dahroug, S., Metwally, A.M., 2023. Detection of karst features and associated geohazard using ground penetrating radar and 2D electrical resistivity imaging; case study from Sannur Protectorate, Egypt. Contrib. Geophys. Geod. 53, 167–190–167–190. https://doi.org/10.31577/congeo.2023.53.3.1.

Hoerl, A.E., Kennard, R.W., 1970. Ridge regression: Biased estimation for nonorthogonal problems. Technometrics 12, 55–67. https://doi.org/10.1080/00401706.1970.10488634.

Hu, N., Wang, M., Qiu, B., Tao, Y., 2022. Numerical simulation of elastic wave field in viscoelastic two-phasic porous materials based on constant Q fractional-order BISQ model. Materials 15, 1020. https://doi.org/10.3390/ma15031020.

Huang, G., Chen, X., Luo, C., Chen, Y., 2021. Dynamic characterization of reservoirs constrained by time-lapse prestack seismic inversion. IEEE Trans. Geosci. Remote Sensing 59, 5549–5562. https://doi.org/10.1109/TGRS.2020.3019526.

Jin, Z., Chapman, M., Papageorgiou, G., 2018. Frequency-dependent anisotropy in a partially saturated fractured rock. Geophys. J. Int. 215, 1985–1998. https://doi.org/10.1093/gji/ggy399.

Kouadio, K.L., Liu, R., Mi, B., Liu, C., 2022. pyCSAMT: an alternative python toolbox for groundwater exploration using controlled source audio-frequency magnetotelluric. J. Appl. Geophys. 201, 104647. https://doi.org/10.1016/j.jappgeo.2022.104647.

Li, Y., Guo, Z., Liu, C., 2024. Characterization of fluid-saturated fractures based on seismic azimuthal anisotropy dispersion inversion method. IEEE Trans. Geosci. Remote Sens. 62, 1–17. https://doi.org/10.1109/TGRS.2024.3407134.

Luo, X., Chen, X., Lv, B., Liu, J., Wu, H., Wang, P., 2023. Frequency-dependent AVO inversion using a modified window-parameter-optimized S-transform for high gas-saturation reservoir delineation. IEEE Geosci. Remote Sens. Lett. 20, 1–5. https://doi.org/10.1109/LGRS.2023.3243846.

Makarian, E., Elyasi, A., Moghadam, R.H., Khoramian, R., Namazifard, P., 2023. Rock physics-based analysis to discriminate lithology and pore fluid saturation of carbonate reservoirs: a case study. Acta Geophys. 71, 2163–2180. https://doi.org/10.1007/s11600-023-01029-0.

Mavko, G., Nur, A., 1975. Melt squirt in the asthenosphere. J. Geophys. Res. 80, 1444–1448. https://doi.org/10.1029/JB080i011p01444.

Mavko, G., Mukerji, T., Dvorkin, J., 2020. The Rock Physics Handbook, 3rd ed. Cambridge University Press. https://doi.org/10.1017/9781108333016.

Metwally, A.M., Mabrouk, W.M., Mahmoud, A.I., 2022. A numerical approach to accurately estimate water resistivity (rw) and saturation (sw) in shaly sand formations. Contrib. Geophys. Geod. 52, 423–441. https://doi.org/10.31577/congeo.2022.52.3.4.

Miao, F., He, Y.-X., Ni, J., Yuan, S., Wang, S., 2025. A novel approach of frequency-dependent seismic elastic parameters inversion for fluid prediction at thin sandstone reservoirs. IEEE Geosci. Remote Sens. Lett. 22, 1–5. https://doi.org/10.1109/LGRS.2024.3510579.

Mondol, N.H., Bjørlykke, K., Jahren, J., Høeg, K., 2007. Experimental mechanical compaction of clay mineral aggregates—changes in physical properties of mudstones during burial. Mar. Pet. Geol. 24, 289–311. https://doi.org/10.1016/j.marpetgeo.2007.03.006.

Müller, T.M., Gurevich, B., Lebedev, M., 2010. Seismic wave attenuation and dispersion resulting from wave-induced flow in porous rocks — a review. Geophysics 75, 75A147–75A164. https://doi.org/10.1190/1.3463417.

Ouyang, F., Liu, X.-Z., Wang, B., Hu, Z.-D., Zhao, J.-G., Yan, X.-Y., Zhang, Y., Qing, Y.-H., 2023. The applicability and underlying factors of frequency-dependent amplitude-

versus-offset (AVO) inversion. Pet. Sci. 20, 2075–2091. https://doi.org/10.1016/j.petsci.2023.02.011.
Pang, M., Ba, J., Carcione, J.M., Picotti, S., Zhou, J., Jiang, R., 2019. Estimation of porosity and fluid saturation in carbonates from rock-physics templates based on seismic Q. Geophysics 84, M25–M36. https://doi.org/10.1190/geo2019-0031.1.
Ran, S., Shen, J., Long, G., Hu, Z., Zhang, C., Zhang, J., 2025. Influence of metal infrastructure on transient electromagnetic detection and effective measurement methods in complex tunnel environments. J. Appl. Geophys. 241, 105787. https://doi.org/10.1016/j.jappgeo.2025.105787.
Ritchie, H., Holman, I., Nyangoka, J., Bauman, P., Parker, A., 2024. Insights from electrical resistivity tomography on the hydrogeological interaction between sand dams and the weathered basement aquifer. J. Appl. Geophys. 230, 105542. https://doi.org/10.1016/j.jappgeo.2024.105542.
Saleh, K., El Hameedy, M.A., Mabrouk, W.M., Metwally, A., 2025a. XGBoost regression for robust acoustic impedance prediction in the absence of density and sonic logs. Sci. Rep. 15, 40388. https://doi.org/10.1038/s41598-025-24727-9.
Saleh, K., Mabrouk, W.M., Metwally, A., 2025b. Machine learning model optimization for compressional sonic log prediction using well logs in shahd SE field, western desert, Egypt. Sci. Rep. 15, 14957. https://doi.org/10.1038/s41598-025-97938-9.
Saleh, K., Mabrouk, W.M., Metwally, A.M., 2025c. Convolutional neural network approach for automated well zonation in the lower bahariya member north western desert Egypt. Sci. Rep. 16, 625. https://doi.org/10.1038/s41598-025-32119-2.
Saltelli, A., 2002. Making best use of model evaluations to compute sensitivity indices. Comput. Phys. Commun. 145, 280–297. https://doi.org/10.1016/S0010-4655(02)00280-1.
She, J., Zou, G., Gong, F., Zeng, H., Liu, Y., Teng, D., Li, J., 2024. Predicting sandstone water abundance using seismic dispersion attribute inversion: a case study of yuwang coal mine. China. Geophys. Prospect. 72, 2357–2376. https://doi.org/10.1111/1365-2478.13515.
Sobol', I.M., 2001. Global sensitivity indices for nonlinear mathematical models and their Monte Carlo estimates. Math. Comput. Simul., The Second IMACS Seminar on Monte Carlo Methods 55, 271–280. https://doi.org/10.1016/S0378-4754(00)00270-6.
Strack, K.M., 2014. Future directions of electromagnetic methods for hydrocarbon applications. Surv. Geophys. 35, 157–177. https://doi.org/10.1007/s10712-013-9237-z.
Su, C., Liu, C., Liu, Y., Ma, G., Gao, X., Wang, Y., Zhang, B., 2024. High-resolution hybrid-dimensional inversion of transient electromagnetic data for water hazard detection in coal mines. IEEE Trans. Geosci. Remote Sensing 62, 1–14. https://doi.org/10.1109/TGRS.2024.3447285.
Sun, Y., Carcione, J.M., Gurevich, B., 2020. Squirt-flow seismic dispersion models: a comparison. Geophys. J. Int. 222, 2068–2082. https://doi.org/10.1093/gji/ggaa274.
Tisato, N., Madonna, C., 2012. Attenuation at low seismic frequencies in partially saturated rocks: Measurements and description of a new apparatus. J. Appl. Geophys. 86, 44–53. https://doi.org/10.1016/j.jappgeo.2012.07.008.
Tisato, N., Quintal, B., 2013. Measurements of seismic attenuation and transient fluid pressure in partially saturated berea sandstone: evidence of fluid flow on the mesoscopic scale. Geophys. J. Int. 195, 342–351. https://doi.org/10.1093/gji/ggt259.
Tisato, N., Madonna, C., Saenger, E.H., 2021. Attenuation of seismic waves in partially saturated berea sandstone as a function of frequency and confining pressure. Front. Earth Sci. 9, 641177. https://doi.org/10.3389/feart.2021.641177.
Wang, Yao, Wang, Yanfei, 2023. Quantitative evaluation of gas hydrate reservoir by AVO attributes analysis based on the brekhovskikh equation. Pet. Sci. 20, 2045–2059. https://doi.org/10.1016/j.petsci.2023.02.008.
Wang, D., Sui, W., Ranville, J.F., 2022. Hazard identification and risk assessment of groundwater inrush from a coal mine: a review. Bull. Eng. Geol. Environ. 81, 421. https://doi.org/10.1007/s10064-022-02925-3.
Wei, lele, Gan, L., Qian, D., ZhiFang, Y., DaXing, W., Xin, Z., Hao, Y., XiaoYue, Z., 2023. Response characteristic analysis and inversion method of mobility based on White's layered patchy-saturated model. Chin. J. Geophys. 66, 2611–2620. https://doi.org/10.6038/cjg2022P0952.
Wei, Q., Han, D.-H., Li, H., Wang, J., Wang, Y., Chen, J., 2024. Effects of fluid saturation and viscosity on seismic dispersion characteristics in berea sandstone. Geophysics 89, MR251–MR263. https://doi.org/10.1190/geo2023-0350.1.
White, J.E., 1975. Computed seismic speeds and attenuation in rocks with partial gas saturation. Geophysics 40, 224–232. https://doi.org/10.1190/1.1440520.
Wood, A.B., Lindsay, R.B., 1956. A textbook of sound. Phys. Today 9, 37. https://doi.org/10.1063/1.3059819.
Wu, X., Liu, T., 2009. Spectral decomposition of seismic data with reassigned smoothed pseudo wigner–ville distribution. J. Appl. Geophys. 68, 386–393. https://doi.org/10.1016/j.jappgeo.2009.03.004.
Xue, G., Chen, W., Cheng, J., Liu, S., Yu, J., Lei, K., Guo, W., Feng, X., 2019. A review of electrical and electromagnetic methods for coal mine exploration in China. IEEE Access 7, 177332–177341. https://doi.org/10.1109/ACCESS.2019.2951774.
Yan, J., Wang, E., Xiong, F., 2024. Dispersion characteristics of seismic reflection coefficients in porous media based on the effective biot theory: effect of wave-induced mesoscopic flow. Chin. J. Geophys. 67, 4289–4308. https://doi.org/10.6038/cjg2024R0738.
Yang, D.H., Zhang, Z.J., 2002. Poroelastic wave equation including the biot/squirt mechanism and the solid/fluid coupling anisotropy. Wave Motion 35, 223–245. https://doi.org/10.1016/S0165-2125(01)00106-8.
Yu, H., Chen, T., 2025. Seismic anisotropy of sandstone aquifers in coal seam roofs. COAL GEOLOGY & EXPLORATION 53, 58–67. https://doi.org/10.12363/issn.1001-1986.25.02.0082.
Zhang, X., Guo, Z., Liu, C., 2025. A novel seismic anisotropic dispersion attribute inversion method for fracture characterization in orthorhombic shale gas reservoirs. IEEE Trans. Geosci. Remote Sens. 63, 1–17. https://doi.org/10.1109/TGRS.2025.3579637.
Zhao, D., Liu, C., Guo, Z., 2023. Estimation of interlayer elastic dispersion attributes based on a new frequency- dependent elastic impedance inversion method. IEEE Trans. Geosci. Remote Sens. 61, 1–11. https://doi.org/10.1109/TGRS.2023.3329514.
Zhu, X., Zong, Z., Zhang, F., 2025. Seismic dispersion-attenuation analysis and hydrocarbon identification within fluid-saturated porous orthorhombic media. IEEE Trans. Geosci. Remote Sens. 63, 1–12. https://doi.org/10.1109/TGRS.2025.3609822.